Journal of Computational Physics 374 (2018) 213–236

Contents lists available at ScienceDirect

Journal of Computational Physics

www.elsevier.com/locate/jcp

Well-balanced positivity preserving central-upwind scheme with a novel wet/dry reconstruction on triangular grids for the Saint-Venant system

Xin Liu [a], Jason Albright [b], Yekaterina Epshteyn [b], Alexander Kurganov [a,c,*]

[a] Department of Mathematics, Southern University of Science and Technology, Shenzhen, 518055, China
[b] Department of Mathematics, The University of Utah, Salt Lake City, UT 84112, USA
[c] Mathematics Department, Tulane University, New Orleans, LA 70118, USA

ARTICLE INFO

Article history:
Received 17 November 2017
Received in revised form 14 May 2018
Accepted 19 July 2018
Available online xxxx

Keywords:
Saint-Venant system of shallow water equations
Central-upwind scheme
Well-balanced scheme
Positivity preserving scheme
Wet/dry reconstruction
Unstructured triangular grid

ABSTRACT

In this paper, we construct an improved well-balanced positivity preserving central-upwind scheme for the two-dimensional Saint-Venant system of shallow water equations. As in Bryson et al. (2011) [7], our scheme is based on a continuous piecewise linear discretization of the bottom topography over an unstructured triangular grid. The main new technique is a special reconstruction of the water surface in partially flooded cells. This reconstruction is an extension of the one-dimensional wet/dry reconstruction from Bollermann et al. (2013) [3]. The positivity of the computed water depth is enforced using the "draining" time-step technique introduced in Bollermann et al. (2011) [4]. The performance of the proposed central-upwind scheme is tested on a number of numerical experiments.

1. Introduction

We consider the two-dimensional (2-D) Saint-Venant system of shallow water equations:

$$h_t + (hu)_x + (hv)_y = 0, \tag{1.1}$$

$$(hu)_t + \left(hu^2 + \frac{g}{2}h^2\right)_x + (huv)_y = -ghB_x, \tag{1.2}$$

$$(hv)_t + (huv)_x + \left(hv^2 + \frac{g}{2}h^2\right)_y = -ghB_y, \tag{1.3}$$

where t is the time, x and y are horizontal spatial coordinates ($(x, y) \in \Omega$), $h(x, y, t)$ is the water depth, $u(x, y, t)$ and $v(x, y, t)$ are the x- and y-components of the flow velocity, $B(x, y)$ is the bottom topography, and g is the constant gravitational acceleration. The system (1.1)–(1.3)was originally proposed in [13], but it is still widely used to model water flow in rivers, lakes, reservoirs, estuaries, and coastal areas.

* Corresponding author.
E-mail addresses: liux7@sustc.edu.cn (X. Liu), ejalbright@lanl.gov (J. Albright), epshteyn@math.utah.edu (Y. Epshteyn), kurganov@math.tulane.edu (A. Kurganov).

In many applications, quasi steady solutions of the system (1.1)–(1.3)are to be computed using a (practically affordable) coarse grid. In such situations, small perturbations of steady states may be amplified by the scheme and the computational errors may become larger than the magnitude of the waves to be captured; see, e.g., [24,32,38]. In order to prevent this, one has to develop a well-balanced scheme—a scheme that is capable of accurately balancing the flux and source terms so that the relevant steady states, for instance, the "lake at rest" steady states,

$$u \equiv v \equiv 0, \quad w := h + B \equiv \text{Const}, \tag{1.4}$$

are preserved within the machine accuracy. Here, w denotes the water surface level. Examples of such schemes can be found in [1,2,4,7,15–17,23,24,28,32,38–42,46].

Another difficulty one often has to face in practice is related to the presence of dry areas (island, shore) in the computational domain. In these areas, $h = 0$ and if due to numerical oscillations h becomes negative, the calculation will simply break down as the acoustic speed needed in the calculation of the eigenvalues of the Jacobians is $\sqrt{gh}$. It is thus crucial for a good scheme to preserve the positivity of h (positivity preserving schemes can be found, e.g., in [1,2,4,7,16,28,39,40,42,46]).

We would also like to point out that in the dry areas, the steady state is

$$hu \equiv hv \equiv h \equiv 0, \tag{1.5}$$

which can be viewed as a "dry lake". A good numerical scheme may be considered "truly" well-balanced when it is capable of exactly preserving both "lake at rest" and "dry lake" steady states, as well as their combinations corresponding to the situations, in which the domain Ω is split into two non-overlapping parts Ω_1 (wet area) and Ω_2 (dry area) and the combined steady-state solution satisfies (1.4)in Ω_1 and (1.5)in Ω_2.

We focus on central-upwind schemes, which were originally developed in [25–27,29–31] for general multidimensional hyperbolic systems of conservation laws. These schemes were extended to hyperbolic systems of balance laws, in particular, to the Saint-Venant system in [2,7,24,28,42]. As in all finite volume Godunov-type schemes, a central-upwind numerical solution realized at a certain time level by a global (in space) piecewise polynomial reconstruction, is evolved to the next time level using the integral form of the system of balance laws. For the second-order schemes, the reconstruction is piecewise linear and the bottom topography is approximated using a continuous piecewise linear (or, in the 2-D schemes on Cartesian grids, piecewise bilinear) interpolant. This allows one to guarantee that the reconstructed water surface stays above the discretized bottom topography, which, in turn, ensures positivity preserving property of the resulting scheme provided a proper CFL condition is satisfied. The well-balanced property is achieved by using an appropriate discretization of the geometric source term.

In order to design a "truly" well-balanced central-upwind scheme for the system (1.1)–(1.3), it is necessary that a piecewise linear reconstruction of the water surface while being positivity preserving respects both the "lake at rest" (1.4) and "dry lake" (1.5) steady-state solutions as well as their combinations. The main difficulty in obtaining such reconstruction is related to the fact that at the wet/dry fronts there are always partially flooded cells, in which the positivity preserving reconstructions from [2,7,28,42] are not well-balanced. A special well-balanced positivity preserving reconstruction for partially flooded cells was developed in [3]for the one-dimensional (1-D) Saint-Venant system. The key idea is to use a subcell resolution, that is, to reconstruct the water surface in some of the partially flooded cells using two (continuously connected) linear pieces instead of one. In this paper, we extend this reconstruction to the 2-D case using unstructured triangular grids. The extension is highly nontrivial since compared to the 1-D case, additional degrees of freedom need to be taken into account and more types of partially flooded cells are to be considered. Moreover, when the new wet/dry reconstruction is used, a new discretization for the source term has to be derived in order to maintain the well-balanced property of the resulting central-upwind scheme. In addition, while the proof of the positivity preserving property from [7]carries over to the new central-upwind scheme, the time-step constraint may be so severe that the scheme would become impractical. We therefore follow the same approach as in [3] and extend the "draining" time-step technique proposed in [4]to the triangular grid. This approach ensures positivity of the computed water depths without a reduction of the time-steps.

The paper is organized as follows. In §2, a modified version of the well-balanced positivity preserving second-order "triangular" central-upwind scheme from [7]is briefly reviewed. In §3, we present the new piecewise linear wet/dry reconstruction. In §4, the positivity preserving property of the new scheme is discussed. In §5, we develop a special discretization of the source term needed to maintain the well-balanced property. Several numerical tests are conducted and the obtained results are presented in §6. Some concluding remarks complete the paper in §7.

2. Semi-discrete central-upwind scheme – an overview

In this section, we describe a slightly modified version of the semi-discrete second-order "triangular" central-upwind scheme from [7].

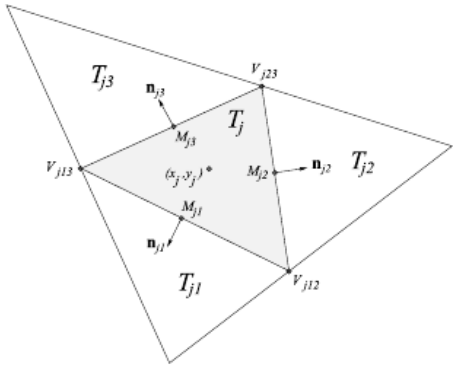

Fig. 2.1. A typical triangular cell with three neighbors.

where the equilibrium variables $\boldsymbol{U}$ and the fluxes $\boldsymbol{F}$ and $\boldsymbol{G}$ are

$$\boldsymbol{U} = \begin{pmatrix} w \\ hu \\ hv \end{pmatrix}, \quad \boldsymbol{F} = \begin{pmatrix} hu \\ \dfrac{(hu)^2}{w-B} + \dfrac{g}{2}(w-B)^2 \\ \dfrac{(hu)(hv)}{w-B} \end{pmatrix}, \quad \boldsymbol{G} = \begin{pmatrix} hv \\ \dfrac{(hu)(hv)}{w-B} \\ \dfrac{(hv)^2}{w-B} + \dfrac{g}{2}(w-B)^2 \end{pmatrix},$$

and the source term $\boldsymbol{S}$ is

$$\boldsymbol{S} = \begin{pmatrix} 0 \\ -g(w-B)B_x \\ -g(w-B)B_y \end{pmatrix}.$$

We use the following notation (illustrated in Fig. 2.1):

$\mathcal{T} := \bigcup_j T_j$ is an unstructured triangulation of the computational domain Ω;
T_j is a triangular cell of size $|T_j|$ with the barycenter (x_j, y_j);
$V_{j\kappa} = (\widetilde{x}_{j\kappa}, \widetilde{y}_{j\kappa})$, $\kappa = 12, 23, 31$ are the three vertices of T_j;
T_{jk}, $k = 1, 2, 3$ are the neighboring triangles that share a common side with T_j;
ℓ_{jk} is the length of the common side of T_j and T_{jk} and M_{jk} is its midpoint;
$\boldsymbol{n}_{jk} := (\cos(\theta_{jk}), \sin(\theta_{jk}))^\top$ is the outer unit normal to the kth side of T_j.

We replace the bottom topography B with its continuous piecewise linear approximation $\widetilde{B}$ given by

$$\begin{vmatrix} x - \widetilde{x}_{j12} & y - \widetilde{y}_{j12} & \widetilde{B}(x,y) - \widehat{B}_{j12} \\ \widetilde{x}_{j23} - \widetilde{x}_{j12} & \widetilde{y}_{j23} - \widetilde{y}_{j12} & \widehat{B}_{j23} - \widehat{B}_{j12} \\ \widetilde{x}_{j13} - \widetilde{x}_{j12} & \widetilde{y}_{j13} - \widetilde{y}_{j12} & \widehat{B}_{j13} - \widehat{B}_{j12} \end{vmatrix} = 0, \quad (x,y) \in T_j,$$

where, in the case of continuous bottom topography, $\widehat{B}_{j\kappa} := B(V_{j\kappa})$ $\kappa = 12, 23, 31$. We then use the following notation:

$$B_{jk} := \widetilde{B}(M_{jk}), \quad B_j := \widetilde{B}(x_j, y_j) = \frac{1}{3}(\widehat{B}_{j12} + \widehat{B}_{j23} + \widehat{B}_{j13}).$$

We assume that at a certain time level t the computed cell averages of the solution,

$$\overline{\boldsymbol{U}}_j(t) \approx \frac{1}{|T_j|} \iint\limits_{T_j} \boldsymbol{U}(x,y,t)\,dxdy,$$

are available. They are then evolved to the next time level by solving the following system of time-dependent ODEs:

$$\frac{d\overline{\boldsymbol{U}}_j}{} = \frac{1}{} \qquad (2.1)$$

$$\begin{aligned}\boldsymbol{H}_{jk} =& \frac{\ell_{jk}\cos(\theta_{jk})}{a^{\text{in}}_{jk}+a^{\text{out}}_{jk}}\Big[a^{\text{in}}_{jk}\boldsymbol{F}(\boldsymbol{U}_{jk}(M_{jk}),B_{jk})+a^{\text{out}}_{jk}\boldsymbol{F}(\boldsymbol{U}_{j}(M_{jk}),B_{jk})\Big]\\ &+\frac{\ell_{jk}\sin(\theta_{jk})}{a^{\text{in}}_{jk}+a^{\text{out}}_{jk}}\Big[a^{\text{in}}_{jk}\boldsymbol{G}(\boldsymbol{U}_{jk}(M_{jk}),B_{jk})+a^{\text{out}}_{jk}\boldsymbol{G}(\boldsymbol{U}_{j}(M_{jk}),B_{jk})\Big]\\ &-\ell_{jk}\frac{a^{\text{in}}_{jk}a^{\text{out}}_{jk}}{a^{\text{in}}_{jk}+a^{\text{out}}_{jk}}\big[\boldsymbol{U}_{jk}(M_{jk})-\boldsymbol{U}_{j}(M_{jk})\big],\quad k=1,2,3.\end{aligned}\tag{2.2}$$

Here, $\boldsymbol{U}_j(M_{jk})$ and $\boldsymbol{U}_{jk}(M_{jk})$ are the reconstructed point values of $\boldsymbol{U}$ at M_{jk} obtained as follows. We first obtain a piecewise linear reconstruction of the variables $\boldsymbol{\Upsilon}:=(w,u,v)^\top$ (rather than $\boldsymbol{U}$ as it was done in [7]):

$$\widetilde{\boldsymbol{\Upsilon}}(x,y)=\sum_j \boldsymbol{\Upsilon}_j(x,y)\chi_{T_j},\quad \boldsymbol{\Upsilon}_j(x,y):=\boldsymbol{\Upsilon}_j+(\widehat{\boldsymbol{\Upsilon}}_x)_j(x-x_j)+(\widehat{\boldsymbol{\Upsilon}}_y)_j(y-y_j),\tag{2.3}$$

where χ_{T_j} is the characteristic function of the cell T_j, $\boldsymbol{\Upsilon}_j$ are the point values of $\boldsymbol{\Upsilon}$ at the cell centers and $(\widehat{\boldsymbol{\Upsilon}}_x)_j$ and $(\widehat{\boldsymbol{\Upsilon}}_y)_j$ are the limited partial derivatives (see §2.1 for the details on their computation).

In order to maintain the numerical stability of the resulting scheme, we prevent appearance of local extrema at the points M_{jk} by setting the slopes of the ith component of $\boldsymbol{\Upsilon}$ to be zero, that is, by taking $(\widehat{\Upsilon}^{(i)}_x)_j=(\widehat{\Upsilon}^{(i)}_y)_j=0$ in (2.3)in those cells T_j, where at least one of the monotonicity conditions,

$$\min\big(\Upsilon^{(i)}_j,\Upsilon^{(i)}_{jk}\big)\le\Upsilon^{(i)}_j(M_{jk})\le\max\big(\Upsilon^{(i)}_j,\Upsilon^{(i)}_{jk}\big),\quad k=1,2,3,$$

is not satisfied.

In the dry cells in which $\overline{w}_j=B_j$, the corresponding linear pieces in (2.3)are replaced by

$$\boldsymbol{\Upsilon}_j(x,y)=(B(x,y),0,0)^\top.\tag{2.4}$$

Finally, the second and third components of the point values $\boldsymbol{U}_j(M_{jk})$ and $\boldsymbol{U}_{jk}(M_{jk})$ are obtained from $\boldsymbol{\Upsilon}_j(M_{jk})$ and $\boldsymbol{\Upsilon}_{jk}(M_{jk})$:

$$\begin{aligned}&(hu)_j(M_{jk})=(w_j(M_{jk})-B_{jk})\,u_j(M_{jk}),\quad (hu)_{jk}(M_{jk})=(w_{jk}(M_{jk})-B_{jk})\,u_{jk}(M_{jk}),\\ &(hv)_j(M_{jk})=(w_j(M_{jk})-B_{jk})\,v_j(M_{jk}),\quad (hv)_{jk}(M_{jk})=(w_{jk}(M_{jk})-B_{jk})\,v_{jk}(M_{jk}).\end{aligned}$$

The cell average of the source term $\boldsymbol{S}_j$ in (2.1),

$$\overline{\boldsymbol{S}}_j(t)\approx\frac{1}{|T_j|}\iint\limits_{T_j}\boldsymbol{S}\big(\boldsymbol{U}(x,y,t),B(x,y)\big)\,dxdy,$$

has to be discretized in a well-balanced manner; see [7]for details. We note that in the presence of dry areas, the quadrature in [7]is not "truly" well-balanced. We therefore have modified it; see §5 below.

In (2.2), a^{in}_{jk} and a^{out}_{jk} are the one-sided local speeds of propagation in the directions $\pm\boldsymbol{n}_{jk}$. These speeds are related to the largest and smallest eigenvalues of the Jacobian matrix $J_{jk}=\cos(\theta_{jk})\frac{\partial\boldsymbol{F}}{\partial\boldsymbol{U}}+\sin(\theta_{jk})\frac{\partial\boldsymbol{G}}{\partial\boldsymbol{U}}$, denoted by $\lambda_+[J_{jk}]$ and $\lambda_-[J_{jk}]$, respectively, and are defined by

$$\begin{aligned}a^{\text{in}}_{jk}&=-\min\{\lambda_-[J_{jk}(\boldsymbol{U}_j(M_{jk}))],\,\lambda_-[J_{jk}(\boldsymbol{U}_{jk}(M_{jk})],\,0\},\\ a^{\text{out}}_{jk}&=\max\{\lambda_+[J_{jk}(\boldsymbol{U}_j(M_{jk}))],\,\lambda_+[J_{jk}(\boldsymbol{U}_{jk}(M_{jk})],\,0\},\end{aligned}$$

where

$$\begin{aligned}\lambda_\pm[J_{jk}(\boldsymbol{U}_j(M_{jk}))]&=\cos(\theta_{jk})u_j(M_{jk})+\sin(\theta_{jk})v_j(M_{jk})\pm\sqrt{gh_j(M_{jk})},\\ \lambda_\pm[J_{jk}(\boldsymbol{U}_{jk}(M_{jk}))]&=\cos(\theta_{jk})u_{jk}(M_{jk})+\sin(\theta_{jk})v_{jk}(M_{jk})\pm\sqrt{gh_{jk}(M_{jk})}.\end{aligned}$$

Remark 2.1. In order to avoid division by 0 (or by a very small positive number), the numerical flux (2.2)is replaced with

$$\boldsymbol{H}_{jk}=\frac{\ell_{jk}\cos(\theta_{jk})}{2}\big[\boldsymbol{F}(\boldsymbol{U}_{jk}(M_{jk}),B_{jk})+\boldsymbol{F}(\boldsymbol{U}_{j}(M_{jk}),B_{jk})\big]$$

$$+\ell_{jk}\sin(\theta_{jk})$$

Remark 2.2. A fully discrete scheme can be obtained by numerically solving the ODE system (2.1), (2.2)using a stable and sufficiently accurate ODE solver. In our numerical experiments, we have used the three-stage third-order strong stability preserving (SSP) Runge–Kutta method; see, e.g., [18,19]. The time-step size should satisfy the CFL condition (see [27]), which can be expressed as

$$\Delta t < \frac{1}{3}\min_{j,k}\left[\frac{r_{jk}}{\max(a^{\text{in}}_{jk}, a^{\text{out}}_{jk})}\right], \tag{2.5}$$

where r_{j1}, r_{j2} and r_{j3} are the three corresponding altitudes of the triangle T_j.

2.1. Computing point values at the cell centers and gradients

We first obtain the point values $\boldsymbol{\Upsilon}_j$ required in formula (2.3). Since our scheme is (formally) second-order accurate in space, we set the cell center point values of all of the evolved quantities to be equal to their computed cell averages. In order to compute the cell center point values of the velocities, $u_j \approx u(x_j, y_j, t)$ and $v_j \approx v(x_j, y_j, t)$, we use the following desingularization procedure (which is different from the one used in [7]):

$$u_j = \begin{cases} \dfrac{(\overline{hu})_j}{\bar{h}_j}, & \text{if } \bar{h}_j \ge \varepsilon, \\ \dfrac{\sqrt{2}\bar{h}_j(\overline{hu})_j}{\sqrt{\bar{h}_j^4 + \max(\bar{h}_j^4, \tau)}}, & \text{otherwise,} \end{cases} \qquad v_j = \begin{cases} \dfrac{(\overline{hv})_j}{\bar{h}_j}, & \text{if } \bar{h}_j \ge \varepsilon, \\ \dfrac{\sqrt{2}\bar{h}_j(\overline{hv})_j}{\sqrt{\bar{h}_j^4 + \max(\bar{h}_j^4, \tau)}}, & \text{otherwise,} \end{cases} \tag{2.6}$$

where $\varepsilon > 0$ and $\tau > 0$ are prescribed small parameters: $\varepsilon > 0$ represents the depth-tolerance used to switch the velocity desingularization on and τ is used to avoid division by very small numbers.

The slopes $(\widehat{\boldsymbol{\Upsilon}}_x)_j$ and $(\widehat{\boldsymbol{\Upsilon}}_y)_j$ in (2.3)are computed in a component-wise manner using the nonlinear limiter from [22]. To this end, we denote a component of $\boldsymbol{\Upsilon}$ by Υ and first compute the unlimited gradients $(\nabla\Upsilon)_j = \big((\Upsilon_x)_j, (\Upsilon_y)_j\big)$ in every cell T_j by taking the x- and y-derivatives of the planes passing through $(x_{j1}, y_{j1}, \Upsilon_{j1})$, $(x_{j2}, y_{j2}, \Upsilon_{j2})$ and $(x_{j3}, y_{j3}, \Upsilon_{j3})$ at three neighboring cell centers:

$$\begin{aligned} (\Upsilon_x)_j &= \frac{(y_{j3}-y_{j1})(\Upsilon_{j2}-\Upsilon_{j1}) - (y_{j2}-y_{j1})(\Upsilon_{j3}-\Upsilon_{j1})}{(y_{j3}-y_{j1})(x_{j2}-x_{j1}) - (y_{j2}-y_{j1})(x_{j3}-x_{j1})}, \\ (\Upsilon_y)_j &= \frac{(x_{j2}-x_{j1})(\Upsilon_{j3}-\Upsilon_{j1}) - (x_{j3}-x_{j1})(\Upsilon_{j2}-\Upsilon_{j1})}{(x_{j2}-x_{j1})(y_{j3}-y_{j1}) - (x_{j3}-x_{j1})(y_{j2}-y_{j1})}. \end{aligned} \tag{2.7}$$

The limited slopes are then given by

$$\begin{aligned} (\widehat{\Upsilon}_x)_j &= \Lambda_{j1}(\Upsilon_x)_{j1} + \Lambda_{j2}(\Upsilon_x)_{j2} + \Lambda_{j3}(\Upsilon_x)_{j3}, \\ (\widehat{\Upsilon}_y)_j &= \Lambda_{j1}(\Upsilon_y)_{j1} + \Lambda_{j2}(\Upsilon_y)_{j2} + \Lambda_{j3}(\Upsilon_y)_{j3}, \end{aligned}$$

where Λ_{j1}, Λ_{j2} and Λ_{j3} are the weights defined by

$$\begin{aligned} \Lambda_{j1} &= \frac{\|(\nabla\Upsilon)_{j2}\|_2^2\,\|(\nabla\Upsilon)_{j3}\|_2^2 + \eta}{\|(\nabla\Upsilon)_{j1}\|_2^4 + \|(\nabla\Upsilon)_{j2}\|_2^4 + \|(\nabla\Upsilon)_{j3}\|_2^4 + 3\eta}, \\ \Lambda_{j2} &= \frac{\|(\nabla\Upsilon)_{j1}\|_2^2\,\|(\nabla\Upsilon)_{j3}\|_2^2 + \eta}{\|(\nabla\Upsilon)_{j1}\|_2^4 + \|(\nabla\Upsilon)_{j2}\|_2^4 + \|(\nabla\Upsilon)_{j3}\|_2^4 + 3\eta}, \\ \Lambda_{j3} &= \frac{\|(\nabla\Upsilon)_{j1}\|_2^2\,\|(\nabla\Upsilon)_{j2}\|_2^2 + \eta}{\|(\nabla\Upsilon)_{j1}\|_2^4 + \|(\nabla\Upsilon)_{j2}\|_2^4 + \|(\nabla\Upsilon)_{j3}\|_2^4 + 3\eta}. \end{aligned}$$

Here, the parameter η is a small positive number introduced to prevent division by zero. In our numerical experiments, we have used $\eta = 10^{-14}$.

2.2. Positivity correction for the reconstructed water surface

Notice that the use of the limited piecewise linear reconstruction (2.3)(with the slopes calculated as described in §2.1 or using another limiter) cannot guarantee that the reconstructed water surface $w_j(x, y)$ stays above the corresponding

In [7], the following positivity correction was performed in the two possible Cases $\mathcal{A}$ and $\mathcal{B}$.

• Case $\mathcal{A}$. There is only one vertex in the cell T_j, say, with index $\kappa = 12$, for which $w_j(V_{j\kappa}) < \widehat{B}_{j\kappa}$. In this case, we first set $w_j(V_{j12}) = \widehat{B}_{j12}$ and then determine $w_j(V_{j23})$ and $w_j(V_{j31})$ at the remaining two vertices by setting $w_j(V_{j23}) - \widehat{B}_{j23} = w_j(V_{j31}) - \widehat{B}_{j31} = \frac{3}{2}(\overline{w}_j - B_j)$ based on the mass conservation. Finally, the original reconstruction (2.3)for w is replaced in the cell T_j with a new one (still denoted by $w_j(x, y)$) defined by

$$\begin{vmatrix} x - x_j & y - y_j & w_j(x, y) - \overline{w}_j \\ \widetilde{x}_{j12} - x_j & \widetilde{y}_{j12} - y_j & \widehat{B}_{j12} - \overline{w}_j \\ \widetilde{x}_{j23} - x_j & \widetilde{y}_{j23} - y_j & \frac{3}{2}(\overline{w}_j - B_j) + \widehat{B}_{j23} - \overline{w}_j \end{vmatrix} = 0, \quad (x, y) \in T_j. \tag{2.8}$$

• Case $\mathcal{B}$. There are two vertices in the cell T_j, say, with indices $\kappa = 12$ and 23, for which $w_j(V_{j\kappa}) < \widehat{B}_{j\kappa}$. In this case, we first set $w_j(V_{j12}) = \widehat{B}_{j12}$ and $w_j(V_{j23}) = \widehat{B}_{j23}$ and then the conservation requirement yields $w_j(V_{j31}) - \widehat{B}_{j31} = 3(\overline{w}_j - B_j)$. Finally, the original reconstruction (2.3)for w is replaced with a new one (still denoted by $w_j(x, y)$) defined by

$$\begin{vmatrix} x - x_j & y - y_j & w_j(x, y) - \overline{w}_j \\ \widetilde{x}_{j12} - x_j & \widetilde{y}_{j12} - y_j & \widehat{B}_{j12} - \overline{w}_j \\ \widetilde{x}_{j23} - x_j & \widetilde{y}_{j23} - y_j & \widehat{B}_{j23} - \overline{w}_j \end{vmatrix} = 0, \quad (x, y) \in T_j. \tag{2.9}$$

One can easily see that the linear pieces (2.8) and (2.9)are conservative and lead to non-negativity of the reconstructed point values of water depth throughout the entire cell T_j. However, in the presence of wet/dry fronts, the reconstruction procedure (2.3), (2.4), (2.8) and (2.9)can not guarantee the well-balanced property at the wet/dry interfaces. We therefore propose a novel wet/dry reconstruction (§3) together with a special discretization of the source term (§5) to maintain the well-balanced property in the presence of dry areas.

3. A novel well-balanced wet/dry reconstruction

In this section, we propose a novel conservative well-balanced wet/dry reconstruction on unstructured triangular grids. This reconstruction can be viewed as an extension of the 1-D wet/dry reconstruction from [3].

Assuming at a certain time level t, $\overline{w}_j \geq B_j$ for all j, we define the following three types of computational cells:

• *Fully flooded cell.* If $\overline{w}_j$ is not lower than the bed level at all three vertices of T_j, that is, if $\overline{w}_j \geq \max(\widehat{B}_{j12}, \widehat{B}_{j23}, \widehat{B}_{j31})$ and $\overline{h}_j := \overline{w}_j - B_j > 0$, the cell is fully flooded.

• *Partially flooded cell.* If $\overline{w}_j$ is lower than the maximum bed level in T_j, that is, if $B_j < \overline{w}_j < \max(\widehat{B}_{j12}, \widehat{B}_{j23}, \widehat{B}_{j31})$, the cell is partially flooded.

• *Dry cell.* If $\overline{w}_j = B_j$, the cell is dry.

We first recall that in partially flooded and dry cells, even the first-order piecewise constant reconstruction of the water surface (equilibrium) variable w may lead to appearance of negative water depth point values as illustrated in Fig. 3.1 (left), in which $h_{j\kappa} = w_{j\kappa} - \widehat{B}_{j\kappa} < 0$. The correction algorithm proposed in [7](see §2.2) can guarantee the positivity of the reconstructed water depth point values. Such correction, however, cannot guarantee the well-balanced property as illustrated in Fig. 3.1 (right), where one can see that the reconstructed values $w_j(M_{jk})$ and $w_{jk}(M_{jk})$ are not guaranteed to be the same for a "lake at rest" steady state.

To overcome the aforementioned difficulties, we develop an alternative correction procedure, which is both positivity preserving and well-balanced even on "dry lake" steady states.

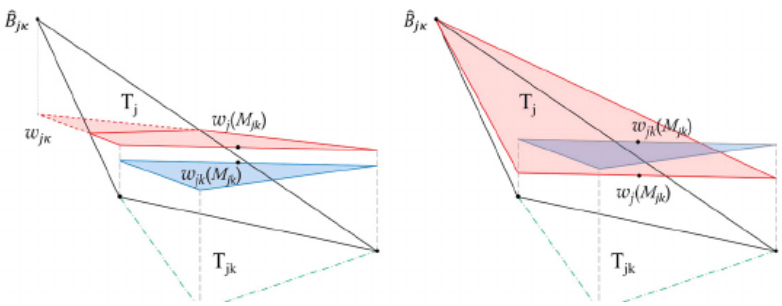

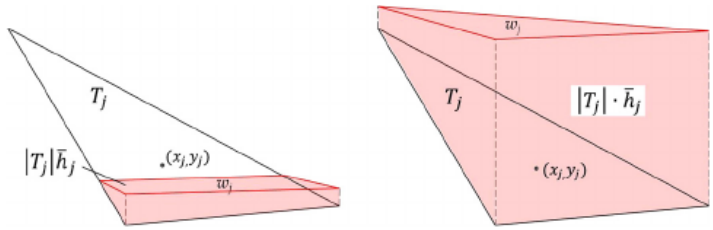

Fig. 3.2. Well-balance first-order water surface reconstruction in partially (left) and fully (right) flooded cells.

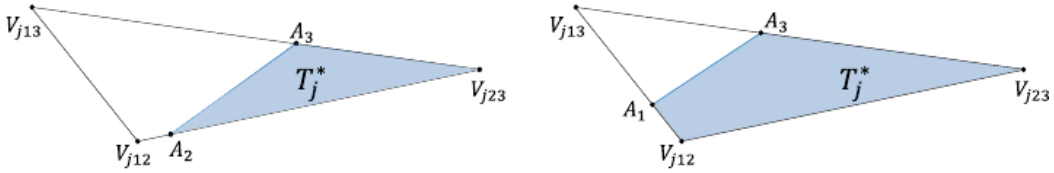

Fig. 3.3. Two types of partially flooded cells depending on the total amount of water in the cell.

3.1. Well-balanced first-order water surface reconstruction

We first introduce a first-order water surface reconstruction, which keeps the water surface flat in a non-dry part of the cell. This reconstruction is illustrated in Fig. 3.2 for typical partially (left) and fully (right) flooded cells.

If T_j is a dry cell, then the water surface is approximated there by

$$w_j(x,y) = \widetilde{B}(x,y).$$

If T_j is a fully flooded cell, then the first-order reconstruction is simply

$$w_j(x,y) = \overline{w}_j.$$

If T_j is a partially flooded cell, then the well-balanced nonnegative first-order approximation of w consists of two pieces—the constant and linear ones:

$$w_j(x,y) = \begin{cases} w_j, & \text{if } (x,y) \in T_j^*, \\ \widetilde{B}(x,y), & \text{otherwise.} \end{cases} \tag{3.1}$$

Here, T_j^* is the flooded area of the partially flooded cell T_j under the horizontal water surface at level w_j, chosen in such way that the volume of water enclosed between the surface $w = w_j$ and the bottom topography equals to the total amount of water in this cell, that is, to $|T_j|\bar{h}_j$.

From now on, we will consider (without loss of generality) partially flooded cells with either $\widehat{B}_{j13} \geq \widehat{B}_{j12} > \widehat{B}_{j23}$ and distinguish between the following two types of such cells depending on the total amount of water in the cell.

Type 1. There exist two points A_2 and A_3 such that $\widehat{B}_{j13} \geq \widehat{B}_{j12} \geq w_j = \widetilde{B}(A_2) = \widetilde{B}(A_3) > \widehat{B}_{j23}$ and thus the area T^* is a triangle as outlined in Fig. 3.3 (left);

Type 2. There exist two points A_1 and A_3 such that $\widehat{B}_{j13} > w_j = \widetilde{B}(A_1) = \widetilde{B}(A_3) > \widehat{B}_{j12} > \widehat{B}_{j23}$ and thus the area T^* is a quadrilateral as outlined in Fig. 3.3 (right).

In Type 1 partially flooded cells, the total amount of water is

$$|T_j|\bar{h}_j = \frac{w_j - \widehat{B}_{j23}}{3}|T_j^*|, \tag{3.2}$$

and since simple similarity consideration gives

$$\frac{|T_j^*|}{|T_j|} = \frac{|A_3V_{j23}|\cdot|A_2V_{j23}|}{|V_{j13}V_{j23}|\cdot|V_{j12}V_{j23}|} = \frac{(w_j - \widehat{B}_{j23})^2}{(\widehat{B}_{j13} - \widehat{B}_{j23})(\widehat{B}_{j12} - \widehat{B}_{j23})},$$

we obtain from (3.2) that

$$\bar{h}_j = \frac{(w_j - \widehat{B}_{j23})^3}{3(\widehat{B}_{j13} - \widehat{B}_{j23})(\widehat{B}_{j12} - \widehat{B}_{j23})}. \tag{3.3}$$

$$\overline{w}_j \le \widehat{B}_{j12} + \frac{(\widehat{B}_{j13} - \widehat{B}_{j12})^2}{3(\widehat{B}_{j13} - \widehat{B}_{j23})}, \tag{3.4}$$

and the value of w_j in this case is also obtained from (3.3) and is given by

$$w_j = \widehat{B}_{j23} + \left[3\bar{h}_j(\widehat{B}_{j13} - \widehat{B}_{j23})(\widehat{B}_{j12} - \widehat{B}_{j23})\right]^{\frac{1}{3}}.$$

In Type 2 partially flooded cells, which according to (3.4)are characterized by the following inequality:

$$\widehat{B}_{j12} + \frac{(\widehat{B}_{j13} - \widehat{B}_{j12})^2}{3(\widehat{B}_{j13} - \widehat{B}_{j23})} < \overline{w}_j < \widehat{B}_{j13},$$

the total amount of water is

$$|T_j|\bar{h}_j = \frac{w_j - \widehat{B}_{j23}}{3}|A_1A_3V_{j23}| + \frac{w_j - \widehat{B}_{j12} + w_j - \widehat{B}_{j23}}{3}|A_1V_{j12}V_{j23}|. \tag{3.5}$$

Note that in this calculation, the quadrilateral $|T_j^*|$ is split into the two triangles, $A_1A_3V_{j23}$ and $A_1V_{j12}V_{j23}$, and then we once again use simple similarity considerations that give

$$\frac{|A_1A_3V_{j23}|}{|T_j|} = \frac{|A_1A_3V_{j23}|}{|A_1V_{j13}V_{j23}|}\cdot\frac{|A_1V_{j13}V_{j23}|}{|T_j|} = \frac{|A_3V_{j23}|}{|V_{j13}V_{j23}|}\cdot\frac{|V_{j13}A_1|}{|V_{j13}V_{j12}|} = \frac{w_j - \widehat{B}_{j23}}{\widehat{B}_{j13} - \widehat{B}_{j23}}\cdot\frac{\widehat{B}_{j13} - w_j}{\widehat{B}_{j13} - \widehat{B}_{j12}}$$

and

$$\frac{|A_1V_{j12}V_{j23}|}{|T_j|} = \frac{|A_1V_{j12}|}{|V_{j13}V_{j12}|} = \frac{w_j - \widehat{B}_{j12}}{\widehat{B}_{j13} - \widehat{B}_{j12}},$$

which are after being substituted into (3.5) result in the following cubic equation for w_j:

$$\begin{aligned} w_j^3 - 3\widehat{B}_{j13}w_j^2 + 3(\widehat{B}_{j23}\widehat{B}_{j13} + \widehat{B}_{j12}\widehat{B}_{j13} - \widehat{B}_{j12}\widehat{B}_{j23})w_j \\ + \left[3\bar{h}_j(\widehat{B}_{j13} - \widehat{B}_{j12}) - \widehat{B}_{j12}(\widehat{B}_{j12} + \widehat{B}_{j23})\right](\widehat{B}_{j13} - \widehat{B}_{j23}) - \widehat{B}_{j23}^2\widehat{B}_{j13} = 0. \end{aligned}$$

Remark 3.1. The obtained quantities $w_j(x, y)$ will be used twofold. Firstly, they will be used in §3.2 to develop a second-order well-balanced piecewise linear water surface reconstruction. Secondly, they are used to modify the computation of the unlimited gradients $(\nabla w)_j = \big((w_x)_j, (w_y)_j\big)^\top$ in (2.7)in the case when the cell T_j is fully flooded, but (at least) one of its neighboring cells T_{jk} is either partially flooded or dry. We note that a straightforward use of (2.7)in such a situation may lead to significant oscillations at wet/dry interfaces and the scheme may fail to preserve "lake at rest" steady states.

In order to overcome this difficulty, we modify formula (2.7)in such problematic cells by replacing the point $(x_{jk}, y_{jk}, \overline{w}_{jk})$ with $\big(M_{jk}, \frac{1}{2}\big[w_j(M_{jk}) + w_{jk}(M_{jk})\big]\big)$ there.

3.2. Well-balanced second-order water surface reconstruction

In this section, we present a new piecewise linear well-balanced nonnegative reconstruction, which is the key component of the proposed new central-upwind scheme. This reconstruction, denoted by $\widetilde{w}^{\,\mathrm{corr}}(x, y) = \sum_{j,k}\widetilde{w}_j^{\,\mathrm{corr}}(x, y)$, can be viewed as a correction of the limited piecewise linear reconstruction $\widetilde{w}(x, y)$ given by (2.3) and described in §2.1 and Remark 3.1.

If T_j is a dry cell, then

$$\widetilde{w}_j^{\,\mathrm{corr}}(x, y) = \widetilde{B}(x, y).$$

If T_j is a fully flooded cell, then no correction is necessary and we set

$$\widetilde{w}_j^{\,\mathrm{corr}}(x, y) = \widetilde{w}_j(x, y).$$

If T_j is a partially flooded cell, then the well-balanced nonnegative second-order approximation of w may consist of two linear pieces:

$$\widetilde{w}_j^{\,\mathrm{corr}}(x, y) = \begin{cases} \mathring{w}_j(x, y), & \text{if } (x, y) \in T_j^*, \\ B(x, y), & \text{otherwise.} \end{cases} \tag{3.6}$$

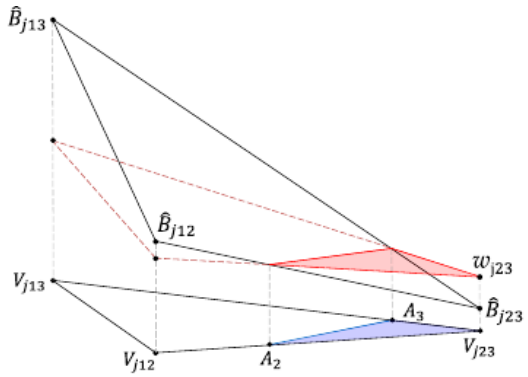

Fig. 3.4. Proposed linear piece $\mathring{w}_j(x,y)$ in **Case 1**.

the definition given in the beginning of §3 the cell T_j is only partially flooded. In such a cease, the corrected reconstruction $\widetilde{w}_j^{\text{corr}}(x,y)$ will consist of one linear piece only; the details will be explained below.

In the remaining part of this section, we describe how to obtain T_j^* and $\mathring{w}_j(x,y)$ in a partially flooded cell. To this end, we first compute the point value w_{j23} at the vertex V_{j23} with lowest bed level in the cell T_j (as in §3.1, we will assume that $\widehat{B}_{j13} \geq \widehat{B}_{j12} \geq \widehat{B}_{j23}$). We will also assume that V_{j23} is a common vertex of m surrounding cells, denoted by $T_{j23}^1, \ldots, T_{j23}^m$ (notice that the studied cell T_j is one of these cells as $V_{j23} \in T_j$), and then take

$$w_{j23} = \max_{1\leq i\leq m} w^i, \quad w^i = \begin{cases} \widetilde{w}_{j23}^i(V_{j23}), & \text{if } T_{j23}^i \text{ is a fully flooded cell,} \\ w_{j23}^i(V_{j23}), & \text{if } T_{j23}^i \text{ is a partially flooded cell,} \\ \widehat{B}_{j23}, & \text{if } T_{j23}^i \text{ is a dry cell,} \end{cases} \quad i = 1, \ldots, m, \tag{3.7}$$

where $\widetilde{w}_{j23}^i(x,y)$ is a linear piece of the reconstruction $\widetilde{w}(x,y)$ in the cell T_{j23}^i and $w_{j23}^i(x,y)$ is the corresponding flat water surface reconstruction (3.1) computed in §3.1.

Equipped with w_{j23} computed in (3.7), we set

$$\mathring{w}_j(V_{j23}) := w_{j23}.$$

We will then distinguish between the following three cases depending on the total amount of water in the partially flooded cell T_j.

Case 1. There exist two points $A_2 = (x_{A_2}, y_{A_2}) \in V_{j12}V_{j23}$ and $A_3 = (x_{A_3}, y_{A_3}) \in V_{j13}V_{j23}$ such that $\widetilde{B}(A_2) = \widetilde{B}(A_3)$ and the total amount of water in the cell T_j is equal to

$$\bar{h}_j|T_j| = \frac{w_{j23} - \widehat{B}_{j23}}{3}|A_2A_3V_{j23}|. \tag{3.8}$$

In this case, T_j^* is a triangle $A_2A_3V_{j23}$, $\mathring{w}_j(A_2) = \widehat{B}_2 := \widetilde{B}(A_2)$, $\mathring{w}_j(A_3) = \widehat{B}_3 := \widetilde{B}(A_3)$, and $\mathring{w}_j(x,y)$, shown in Fig. 3.4, is a linear piece that passes through the following three points: $(A_2, \widehat{B}_2)$, $(A_3, \widehat{B}_3)$ and (V_{j23}, w_{j23}), namely,

$$\begin{vmatrix} x - \widetilde{x}_{j23} & y - \widetilde{y}_{j23} & \mathring{w}_j(x,y) - w_{j23} \\ x_{A_2} - \widetilde{x}_{j23} & y_{A_2} - \widetilde{y}_{j23} & \widehat{B}_2 - w_{j23} \\ x_{A_3} - \widetilde{x}_{j23} & y_{A_3} - \widetilde{y}_{j23} & \widehat{B}_3 - w_{j23} \end{vmatrix} = 0, \quad (x,y) \in T_j^*. \tag{3.9}$$

In order to use (3.9), we need to determine x_{A_2}, y_{A_2}, x_{A_3}, y_{A_3}, $\widehat{B}_2$ and $\widehat{B}_3$. This can be done as follows. First, note that the location of the points A_2 and A_3 can be described using two constants $k_2, k_3 \in (0,1]$ such that $A_2 = k_2V_{j12} + (1-k_2)V_{j23}$ and $A_3 = k_3V_{j13} + (1-k_3)V_{j23}$, and thus by simple similarity considerations

$$\widehat{B}_2 = k_2\widehat{B}_{j12} + (1-k_2)\widehat{B}_{j23}, \quad \widehat{B}_3 = k_3\widehat{B}_{j13} + (1-k_3)\widehat{B}_{j23}, \quad |T_j^*| = k_3k_2|T_j|.$$

This together with (3.8) and the fact that $\widehat{B}_2 = \widehat{B}_3$ result in

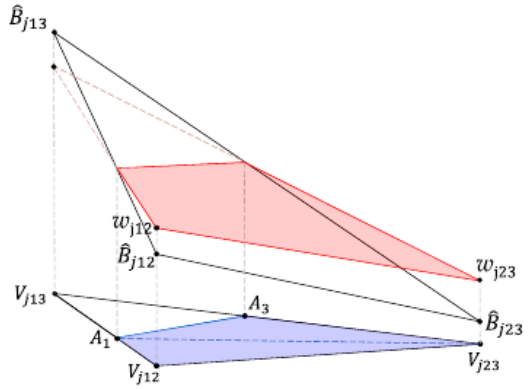

Fig. 3.5. Proposed linear piece $\mathring{w}_j(x, y)$ in **Case 2**.

Since these quantities need to be between 0 and 1, we conclude that Case 1 is characterized by the following condition:

$$0 < \bar{h}_j \le \frac{(\widehat{B}_{j12} - \widehat{B}_{j23})(w_{j23} - \widehat{B}_{j23})}{3(\widehat{B}_{j13} - \widehat{B}_{j23})}. \tag{3.11}$$

Case 2. There exist two points $A_1 = (x_{A_1}, y_{A_1}) \in V_{j13}V_{j12}$ and $A_3 = (x_{A_3}, y_{A_3}) \in V_{j13}V_{j23}$ such that $\widetilde{B}(A_1) = \widetilde{B}(A_3)$ and the total amount of water in the cell T_j is equal to

$$\bar{h}_j|T_j| = \frac{w_{j23} - \widehat{B}_{j23}}{3}|A_1A_3V_{j23}| + \frac{w_{j12} - \widehat{B}_{j12} + w_{j23} - \widehat{B}_{j23}}{3}|A_1V_{j12}V_{j23}|. \tag{3.12}$$

In this case, T_j^* is a quadrilateral $A_1A_3V_{j23}V_{j12}$, $\mathring{w}_j(A_1) = \widehat{B}_1 := \widetilde{B}(A_1)$, $\mathring{w}_j(A_3) = \widehat{B}_3 := \widetilde{B}(A_3)$, and $\mathring{w}_j(x, y)$, shown in Fig. 3.5, is a linear piece that passes through the following three points: $(A_1, \widehat{B}_1)$, $(A_3, \widehat{B}_3)$ and (V_{j23}, w_{j23}), namely,

$$\begin{vmatrix} x - \widetilde{x}_{j23} & y - \widetilde{y}_{j23} & \mathring{w}_j(x, y) - w_{j23} \\ x_{A_1} - \widetilde{x}_{j23} & y_{A_1} - \widetilde{y}_{j23} & \widehat{B}_1 - w_{j23} \\ x_{A_3} - \widetilde{x}_{j23} & y_{A_3} - \widetilde{y}_{j23} & \widehat{B}_3 - w_{j23} \end{vmatrix} = 0, \quad (x, y) \in T_j^*, \tag{3.13}$$

and $w_{j12} := \mathring{w}_j(V_{j12})$.

In order to use (3.13), we need to determine x_{A_1}, y_{A_1}, x_{A_3}, y_{A_3}, $\widehat{B}_1$ and $\widehat{B}_3$. This can be done as follows. First, note that the location of the points A_1 and A_3 can be described using two constants $k_1, k_3 \in (0, 1]$ such that $A_1 = k_1V_{j13} + (1 - k_1)V_{j12}$ and $A_3 = k_3V_{j13} + (1 - k_3)V_{j23}$, and thus by simple similarity considerations

$$\widehat{B}_1 = k_1\widehat{B}_{j13} + (1 - k_1)\widehat{B}_{j12}, \quad \widehat{B}_3 = k_3\widehat{B}_{j13} + (1 - k_3)\widehat{B}_{j23}, \tag{3.14}$$

$$|A_1V_{j12}V_{j23}| = k_1|T_j|, \quad |A_1A_3V_{j23}| = k_3(1 - k_1)|T_j|. \tag{3.15}$$

Note that (3.14) implies that

$$k_3 = 1 - \frac{\widehat{B}_{j12} - \widehat{B}_{j13}}{\widehat{B}_{j23} - \widehat{B}_{j13}}(1 - k_1). \tag{3.16}$$

We then use the similarity considerations once again to obtain

$$\widehat{B}_1 = k_1\mathring{w}_j(V_{j13}) + (1 - k_1)w_{j12} = k_1\widehat{B}_{j13} + (1 - k_1)\widehat{B}_{j12},$$
$$\widehat{B}_3 = k_3\mathring{w}_j(V_{j13}) + (1 - k_3)w_{j23} = k_3\widehat{B}_{j13} + (1 - k_3)\widehat{B}_{j23},$$

which together with the fact that $\widehat{B}_1 = \widehat{B}_3$ gives

$$w_{j12} = \widehat{B}_{j12} + \frac{k_1(1 - k_3)}{k_3(1 - k_1)}(w_{j23} - \widehat{B}_{j23}). \tag{3.17}$$

Next, we substitute (3.14), (3.15) and (3.17)into (3.12), and introduce $\alpha := 3\bar{h}_j/(w_{j23} - \widehat{B}_{j23})$ and $\beta := (\widehat{B}_{j12} - \widehat{B}_{j13})/(\widehat{B}_{j23} - \widehat{B}_{j13})$ and to obtain the following cubic equation for $(1 - k_1)$:

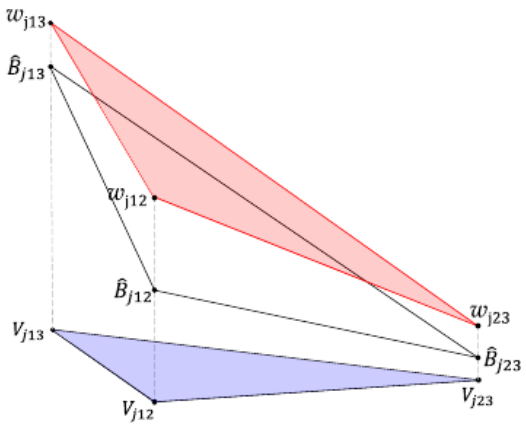

Fig. 3.6. Proposed linear piece $\mathring{w}_j(x, y)$ in **Case 3**.

This equation can be solved analytically. We are interested in a solution $k_1 \in (0, 1]$, which may or may not exist. If it exists (see the discussion below), then k_3 and w_{j12} are obtained from (3.16) and (3.17), respectively.

We note that in the limiting case of $k_1 = 1$, (3.18)results in

$$\bar{h}_j = \frac{2\widehat{B}_{j13} - \widehat{B}_{j23} - \widehat{B}_{j12}}{3(\widehat{B}_{j13} - \widehat{B}_{j23})}(w_{j23} - \widehat{B}_{j23}). \tag{3.19}$$

Using the fact that in this case $\mathring{w}_j(V_{j13}) = \widehat{B}_{j13}$ and thus $3\bar{h}_j = (w_{j23} - \widehat{B}_{j23}) + (w_{j12} - \widehat{B}_{j12})$, we obtain from (3.19) that

$$w_{j12} = w^*_{j12} := \frac{(\widehat{B}_{j13} - \widehat{B}_{j12})}{(\widehat{B}_{j13} - \widehat{B}_{j23})}(w_{j23} - \widehat{B}_{j23}) + \widehat{B}_{j12}. \tag{3.20}$$

Notice that the value w^*_{j12} is introduced here since it will be used in the description of Case 3 below.

Finally, we use (3.11) and (3.19)to conclude that Case 2 is characterized by the following condition:

$$\frac{(\widehat{B}_{j12} - \widehat{B}_{j23})(w_{j23} - \widehat{B}_{j23})}{3(\widehat{B}_{j13} - \widehat{B}_{j23})} \le \bar{h}_j \le \frac{2\widehat{B}_{j13} - \widehat{B}_{j23} - \widehat{B}_{j12}}{3(\widehat{B}_{j13} - \widehat{B}_{j23})}(w_{j23} - \widehat{B}_{j23}). \tag{3.21}$$

Case 3. The third possible case is characterized by the condition, which is complementary to (3.11) and (3.21):

$$\bar{h}_j \ge \frac{2\widehat{B}_{j13} - \widehat{B}_{j23} - \widehat{B}_{j12}}{3(\widehat{B}_{j13} - \widehat{B}_{j23})}(w_{j23} - \widehat{B}_{j23}). \tag{3.22}$$

In this case, $T^*_j = T_j$, and the reconstruction (3.6)over T_j consists of just one linear piece $\mathring{w}_j(x, y)$ given by

$$\begin{vmatrix} x - \widetilde{x}_{j23} & y - \widetilde{y}_{j23} & \mathring{w}_j(x, y) - w_{j23} \\ \widetilde{x}_{j12} - \widetilde{x}_{j23} & \widetilde{y}_{j12} - \widetilde{y}_{j23} & w_{j12} - w_{j23} \\ \widetilde{x}_{j13} - \widetilde{x}_{j23} & \widetilde{y}_{j13} - \widetilde{y}_{j23} & w_{j13} - w_{j23} \end{vmatrix} = 0, \quad (x, y) \in T_j; \tag{3.23}$$

see Fig. 3.6.

In order to use (3.23), we need to determine the values w_{j13} and w_{j12}. This is done by setting

$$w_{j12} = w^*_{j12} + \Delta w, \quad w_{j13} = \widehat{B}_{j13} + \Delta w \tag{3.24}$$

where w^*_{j12} is given by (3.20) and Δw is determined by the conservation requirement:

$$3\bar{h}_j = \Delta w + (\Delta w + w^*_{j12} - \widehat{B}_{j12}) + (w_{j23} - \widehat{B}_{j23}),$$

which results in

3.2.1. Summary of the second-order water surface reconstruction procedure

We now summarize the proposed piecewise linear well-balanced nonnegative reconstruction procedure.

1. Compute the first-order well-balanced nonnegative water surface reconstruction $w_j(x,y)$ as described in §3.1.
2. Compute the unlimited gradients $(\nabla w)_j$ using the method described in Remark 3.1.
3. In each partially flooded cell T_j, compute the water level $w_{j\kappa}$ at the vertex with the lowest bed level in T_j. This is described in (3.7)for the case of the lowest bed level being at the vertex V_{j23} (two alternative possibilities are treated similarly).
4. In each partially flooded cell T_j, determine whether it corresponds to Case 1, 2 or 3 depending on which of the conditions, (3.11), (3.21)or (3.22), respectively, is satisfied.
   - In Case 1, compute k_2 and k_3 using (3.10) and then $\mathring{w}_j(x,y)$ is given by (3.9).
   - In Case 2, compute k_1 and k_3 using (3.18) and (3.16) and then $\mathring{w}_j(x,y)$ is given by (3.13).
   - In Case 3, compute w_{j12} and w_{j13} using (3.20), (3.25) and (3.24) and then $\mathring{w}_j(x,y)$ is given by (3.23).

   Once $\mathring{w}_j(x,y)$ is determined, we obtain $\widetilde{w}_j^{\text{corr}}(x,y)$ using (3.6).
5. Finally, using the corrected piecewise linear reconstruction $\widetilde{w}_j^{\text{corr}}(x,y)$, update the point values $w_{j\kappa}$ and $w_j(M_{jk})$ as well as the piecewise constant gradients $\nabla\widetilde{w}(x,y)$ in partially flooded cells. These new quantities are then used in the numerical scheme described in §2, §4 and §5.

4. Positivity correction of the central-upwind scheme

In order to preserve the positivity of water depth computed using the proposed numerical scheme, we generalize the "draining" time-step method from [3,4] to the triangular mesh used in this paper.

We begin by studying the positivity preserving property of the central-upwind scheme described in §2. To this end, we apply the forward Euler temporal discretization to the first component of the scheme (2.1), (2.2)(the obtained result will also apply to the discretization obtained by the three-stage third-order SSP method used in the numerical examples reported in §6 below):

$$\begin{aligned}\overline{w}_j^{n+1} = \overline{w}_j^{n} &- \frac{\Delta t}{|T_j|}\sum_{k=1}^{3}\frac{\ell_{jk}}{a_{jk}^{\text{in}}+a_{jk}^{\text{out}}}\Big[a_{jk}^{\text{in}}h_{jk}(M_{jk})u_{jk}^{\perp}(M_{jk})+a_{jk}^{\text{out}}h_j(M_{jk})u_j^{\perp}(M_{jk})\Big]\\ &+\frac{\Delta t}{|T_j|}\sum_{k=1}^{3}\ell_{jk}\frac{a_{jk}^{\text{in}}a_{jk}^{\text{out}}}{a_{ik}^{\text{in}}+a_{ik}^{\text{out}}}\big[w_{jk}(M_{jk})-w_j(M_{jk})\big],\end{aligned}\tag{4.1}$$

where $u_j^{\perp}(M_{jk}) := u_j(M_{jk})\cos(\theta_{jk})+v_j(M_{jk})\sin(\theta_{jk})$ and $u_{jk}^{\perp}(M_{jk}) := u_{jk}(M_{jk})\cos(\theta_{jk})+v_{jk}(M_{jk})\sin(\theta_{jk})$. Using the fact that

$$\overline{w}_j^{n+1}-\overline{w}_j^{n}=\bar{h}_j^{n+1}-\bar{h}_j^{n}\quad\text{and}\quad w_{jk}(M_{jk})-w_j(M_{jk})=h_{jk}(M_{jk})-h_j(M_{jk}),$$

the scheme (4.1) can be rewritten as:

$$\begin{aligned}\bar{h}_j^{n+1} = \bar{h}_j^{n} &+ \frac{\Delta t}{|T_j|}\sum_{k=1}^{3}\frac{\ell_{jk}a_{jk}^{\text{in}}}{a_{ik}^{\text{in}}+a_{ik}^{\text{out}}}h_{jk}(M_{jk})\big[a_{jk}^{\text{out}}-u_{jk}^{\perp}(M_{jk})\big]\\ &-\frac{\Delta t}{|T_j|}\sum_{k=1}^{3}\frac{\ell_{jk}a_{jk}^{\text{out}}}{a_{ik}^{\text{in}}+a_{ik}^{\text{out}}}h_j(M_{jk})\big[a_{jk}^{\text{in}}+u_j^{\perp}(M_{jk})\big].\end{aligned}\tag{4.2}$$

For fully flooded cells,

$$\bar{h}_j^{n}=\frac{1}{3}\sum_{k=1}^{3}h_j(M_{jk}),\tag{4.3}$$

which after being substituted into (4.2)leads to the positivity preserving result established in [7]: $\bar{h}_j^{n+1}>0$ provided

$$\Delta t<\frac{1}{6}\min_{j,k}\left[\frac{r_{jk}}{\max(a_{jk}^{\text{in}},a_{jk}^{\text{out}})}\right].\tag{4.4}$$

Notice that this time-step restriction is twice stricter than the one in (2.5)

arbitrarily small. To overcome this numerical difficulty, we use the "draining" time-step technique originally developed in [4], which we extend to unstructured triangular meshes as follows.

We first introduce the "draining" time-step $\Delta t_j^{\text{drain}}$ which represents the minimum time needed for the cell T_j to be completely drained. It is defined by

$$\Delta t_j^{\text{drain}} := \frac{|T_j|\bar{h}_j^n}{\sum_{k=1}^{3} \max(0, H_{jk}^{(1)})}$$

where $H_{jk}^{(1)}$ is the first component of the numerical flux $\boldsymbol{H}_{jk}$ is the numerical flux given by (2.2). Notice that for fully flooded cells $\Delta t_j^{\text{drain}} = \Delta t$, while for dry cells $\Delta t_j^{\text{drain}} = 0$.

We then define the local "draining" time-step Δt_{jk} for each edge ℓ_{jk} of the cell j:

$$\Delta t_{jk} = \begin{cases} \min(\Delta t, \Delta t_j^{\text{drain}}), & \text{if } H_{jk}^{(1)} > 0, \\ \min(\Delta t, \Delta t_{jk}^{\text{drain}}), & \text{if } H_{jk}^{(1)} \le 0, \end{cases}$$

where $\Delta t_{jk}^{\text{drain}}$ is the "draining" time-step in the neighboring cell T_{jk}, and Δt is computed by (4.4), but with the minimum taken there over the flooded cells only.

Finally, equipped with $\Delta t_{jk}^{\text{drain}}$, we replace the forward Euler discretization of (2.1)with

$$\overline{\boldsymbol{U}}_j^{n+1} = \overline{\boldsymbol{U}}_j^n - \frac{1}{|T_j|}\sum_{k=1}^{3} \Delta t_{jk}\boldsymbol{H}_{jk} + \Delta t\,\overline{\boldsymbol{S}}_j. \tag{4.5}$$

One can show that under the time-step restriction (4.4), the scheme (4.5)preserves positivity of h. We omit the proof as it is similar to the proof of the analogous result in [4].

5. Well-balanced discretization of the source terms

In this section, we develop a well-balanced discretization of the source terms, which guarantees that "lake at rest" steady-state solutions,

$$w = \max\{C, B(x,y)\}, \quad C = \text{Const}, \qquad u \equiv v \equiv 0, \tag{5.1}$$

are exactly preserved by the resulting central-upwind scheme in the presence of wet/dry fronts. This means that in both partially and fully flooded cells, the source discretization $\overline{\boldsymbol{S}}_j$ should exactly balance the numerical fluxes so that the right-hand side (RHS) of (2.1) vanishes at "lake at rest" steady states.

To this end, we substitute the "lake at rest" state (5.1)into (2.1), (2.2) and conclude that a well-balanced quadrature for $\overline{\boldsymbol{S}}_j$ should satisfy the following two conditions:

$$-\frac{g}{2|T_j|}\sum_{k=1}^{3} \ell_{jk}\cos(\theta_{jk})\cdot\frac{\Delta t_{jk}}{\Delta t}\cdot\left[C - B(M_{jk})\right]^2 + \overline{S}_j^{(2)} = 0 \tag{5.2}$$

and

$$-\frac{g}{2|T_j|}\sum_{k=1}^{3} \ell_{jk}\sin(\theta_{jk})\cdot\frac{\Delta t_{jk}}{\Delta t}\cdot\left[C - B(M_{jk})\right]^2 + \overline{S}_j^{(3)} = 0, \tag{5.3}$$

where

$$\overline{S}_j^{(2)} \approx -\frac{g}{|T_j|}\iint\limits_{T_j}(C - B(x,y))B_x(x,y)\,dxdy, \quad \overline{S}_j^{(3)} \approx -\frac{g}{|T_j|}\iint\limits_{T_j}(C - B(x,y))B_y(x,y)\,dxdy.$$

In order to derive a well-balanced quadrature, we follow the approach in [7] and first apply Green's formula, $\iint_{T_j}\operatorname{div}\boldsymbol{\mathcal{G}}\,dxdy = \int_{\partial T_j}\boldsymbol{\mathcal{G}}\cdot\boldsymbol{n}\,ds$, to the vector field $\boldsymbol{\mathcal{G}} = (\frac{1}{2}(w(x,y) - B(x,y))^2, 0)$ and obtain

$$-\iint\limits_{T_j}(w(x,y) - B(x,y))B_x(x,y)\,dxdy = \sum_{k=1}^{3}\int\limits_{(\partial T_j)_k}\frac{(w(x,y) - B(x,y))^2}{2}\cos(\theta_{jk})\,ds \tag{5.4}$$

where $(\partial T_j)_k$ is the k-th side of the triangle T_j, $k=1,2,3$. Next, unlike the discretization in [7], which uses the midpoint rule for all of the integrals on the RHS of (5.4), we apply the midpoint rule to the line integrals there, while the double integral is approximated using the trapezoidal rule. This results in the following quadrature for $\overline{S}_j^{(2)}$:

$$\begin{aligned}\overline{S}_j^{(2)} &= \frac{g}{2|T_j|}\sum_{k=1}^{3}\ell_{jk}\cos(\theta_{jk})\cdot\frac{\Delta t_{jk}}{\Delta t}\cdot\Big[w(M_{jk})-B(M_{jk})\Big]^2\\ &\quad-\frac{g}{3}\Big[(w_{j12}-\widehat{B}_{j12})\,w_x(V_{j12})+(w_{j23}-\widehat{B}_{j23})\,w_x(V_{j23})+(w_{j13}-\widehat{B}_{j13})\,w_x(V_{j13})\Big].\end{aligned}\tag{5.5}$$

A similar quadrature for $\overline{S}_j^{(3)}$ is

$$\begin{aligned}\overline{S}_j^{(3)} &= \frac{g}{2|T_j|}\sum_{k=1}^{3}\ell_{jk}\sin(\theta_{jk})\cdot\frac{\Delta t_{jk}}{\Delta t}\cdot\Big[w(M_{jk})-B(M_{jk})\Big]^2\\ &\quad-\frac{g}{3}\Big[(w_{j12}-\widehat{B}_{j12})\,w_y(V_{j12})+(w_{j23}-\widehat{B}_{j23})\,w_y(V_{j23})+(w_{j13}-\widehat{B}_{j13})\,w_y(V_{j13})\Big].\end{aligned}\tag{5.6}$$

Notice that the reconstruction procedure presented in §3.2 ensures that at the steady state (5.1), either $w_{j\kappa}=\widehat{B}_{j\kappa}$ or $\nabla w(V_{j\kappa})=0$ throughout the entire computational domain. This implies that $(w_{j\kappa}-\widehat{B}_{j\kappa})\,w_x(V_{j\kappa})\equiv(w_{j\kappa}-\widehat{B}_{j\kappa})\,w_y(V_{j\kappa})\equiv 0$ and therefore the quadratures (5.5) and (5.6)satisfy the desired well-balanced requirements (5.2) and (5.3).

6. Numerical examples

In this section, we will demonstrate the performance of the developed "truly" well-balanced central-upwind scheme, which will be referred to as a **"new scheme"**, and in Examples 3 and 4, we will also compare the obtained results with the ones computed using the scheme described in §2, which will be referred to as an **"old scheme"**.

In all of the examples, we set the gravitational acceleration to be $g=9.8$ and the desingularization parameters τ and ε in (2.6)are taken to be $\tau=\max_j\{|T_j|^2\}$ and $\varepsilon=10^{-4}$ (except for Example 4, in which we take $\varepsilon=10^{-2}$).

Example 1—Accuracy test

In the first example taken from [47], we test the experimental order of accuracy of the proposed numerical scheme.

We use the following 1-D data,

$$B(x,y)=\sin^2(\pi x),\quad h(x,y,0)=5+e^{\cos(2\pi x)},$$
$$(hu)(x,y,0)=\sin(\cos(2\pi x)),\quad (hv)(x,y,0)\equiv 0,$$

which is artificially extended to the narrow 2-D computational domain $[0,1]\times[-1/(2N),1/(2N)]$, which is first divided into N uniform Cartesian cells, each of which is then split into 4 uniform triangles so that the total number of triangular cells is $N\times 4$. We use the periodic boundary conditions at $x=0$ and $x=1$ and reflecting (solid wall) boundary conditions at the other boundaries.

We compute the solution until the final time $t=0.1$. The reference solution is obtained using 3200×4 cells and then used to compute the L^1-errors and experimental rates of convergence. The results presented in Table 6.1 demonstrate that the expected second order of accuracy is achieved.

Example 2—Dam-break wave propagating over an initially dry inclined plane

In the second test, we compare the performances of the "new scheme" implemented using the proposed first-order §3.1 and second-order §3.2 wet/dry reconstructions in the partially flooded cells at wave fronts. To this end, we capture a dam-break wave over an initially inclined plane. In this test taken from [9,47], the analytical formula for the wave front position is available.

Table 6.1
Example 1: L^1-errors and experimental rates of convergence.

$N\times 4$	h		hu	
	L^1-error	Rate	L^1-error	Rate
50×4	2.43×10^{-3}	–	1.89×10^{-2}	–

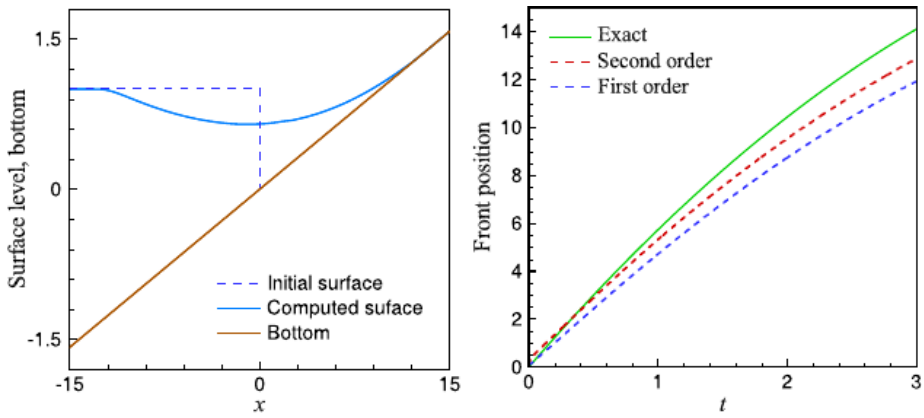

Fig. 6.1. Example 2: $w(x,0,0)$ and $w(x,0,3)$ computed using the second-order wet/dry reconstruction described in §3.2 over the inclined bottom $B(x,0)$ (left); the exact and computed wave front positions, computed using the first- and second-order wet/dry reconstructions (right).

In this test, the initial data are

$$h(x,y,0)=\begin{cases}1-B(x,y), & x<0,\\ 0, & x\geq 0,\end{cases}\qquad u(x,y,0)\equiv v(x,y,0)\equiv 0,$$

and the bottom topography is given by

$$B(x,y)=x\tan(\alpha),$$

where α is the inclination angle, which is set to $\alpha=\pi/30$.

This is a 1-D test, which we artificially extend to the narrow 2-D computational domain $[-15,15]\times[-1/40,1/40]$, which is first divided into 2400 uniform Cartesian cells, each of which is then split into 4 uniform triangles so that the total number of triangular cells is 9600. The reflecting (solid wall) boundary conditions are imposed at all of the boundaries.

According to [9,47], the exact position of the wave front as a function of time is given by

$$x_f(t)=2t\sqrt{g\cos(\alpha)}-\frac{g}{2}t^2\tan(\alpha).$$

We run the simulations until the final time $t=3$. In Fig. 6.1 (left), we plot the cross sections along $y=0$ if the initial and computed (using the second-order wet/dry reconstruction described in §3.2) water surfaces over the inclined bottom. In Fig. 6.1 (right), we show the exact and computed wave fronts as functions of time. As one can clearly see, the "new scheme" implemented using the proposed second-order wet/dry reconstruction §3.2 predicts the wave front position more accurate than the same scheme, but implemented using the first-order wet/dry reconstruction from §3.1.

We would like to stress that in this comparison test, the same piecewise linear reconstructions are used in the fully flooded cells and different wet/dry reconstructions are only applied in partially flooded cells near the wet/dry front. We would also like to point out that the experimental location of the front is defined as the first cell where the water depth exceeds 10^{-4} if counted from the right to the left.

Example 3—"Lake at rest" steady state in the domain with wet/dry interfaces

This test case is designed to demonstrate the well-balanced property of the "new scheme" in the presence of wet/dry interfaces, which is enforced by applying the new well-balanced water surface reconstruction (§3.2) and corresponding discretization of the source terms (§5). To this end, we simulate a quiescent lake around an island using the "new scheme" and compare the obtained results with those computed by the "old scheme".

In this example, we take the computational domain $[0,4]\times[0,2]$ (divided into 12800 triangular cells), the exponential-shape bottom topography

$$B(x,y)=0.8e^{-2(x-2)^2-4(y-1)^2},$$

the "lake at rest" initial data

$$w(x,y,0)=\max(0.5,B(x,y)),\quad u(x,y)\equiv v(x,y)\equiv 0,$$

and reflecting (solid wall) boundary conditions.

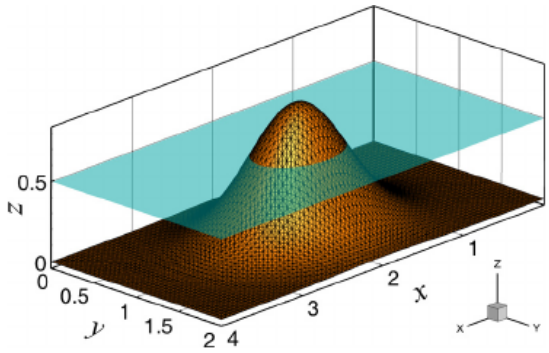

Fig. 6.2. Example 3: Water surface around the partially submerged hump computed using the "new scheme".

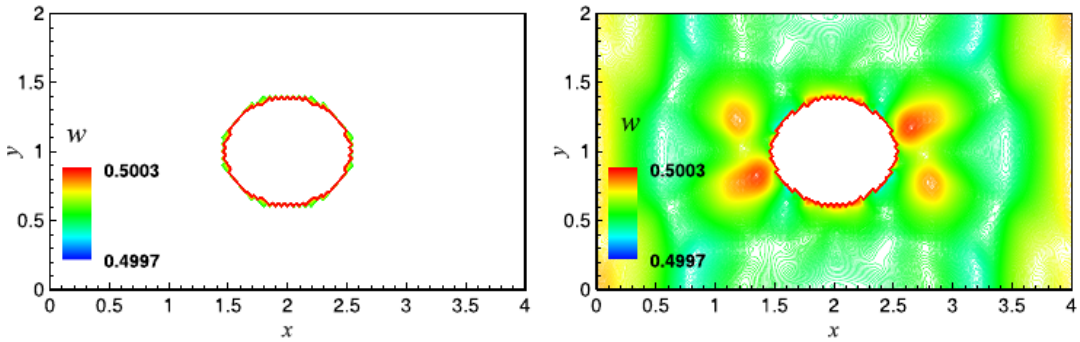

Fig. 6.3. Example 3: Water surface computed by the "new" (left) and "old" (right) schemes. (For interpretation of the colors in the figures, the reader is referred to the web version of this article.)

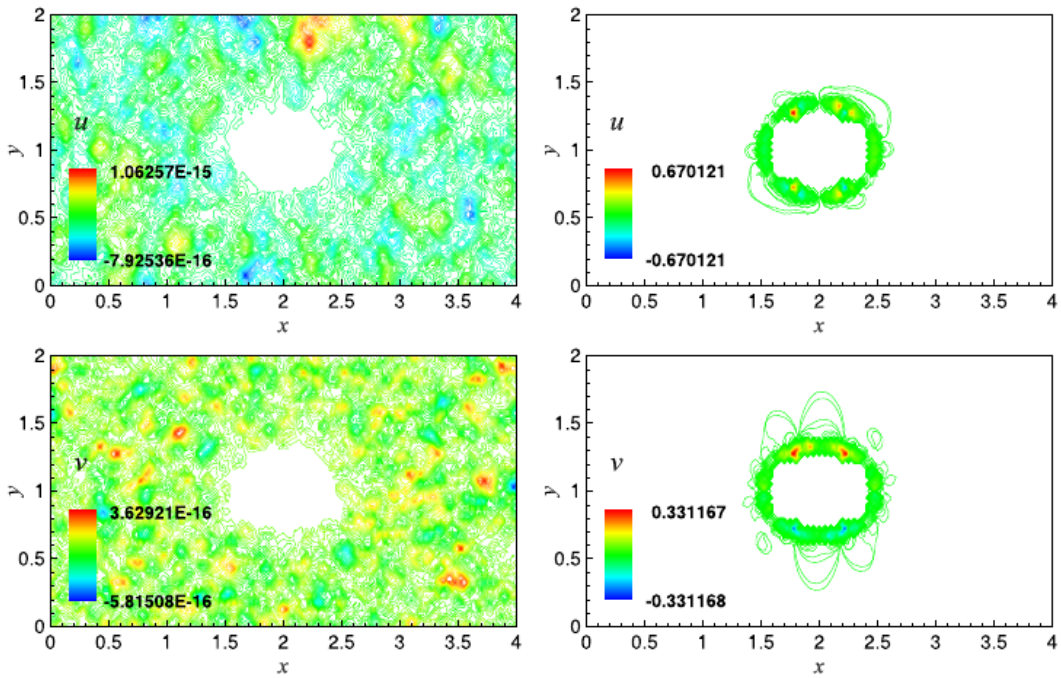

Fig. 6.4. Example 3: Water velocities u (top row) and v (bottom row) computed by the "new" (left column) and "old" (right column) schemes.

We then perform the same computation by the "old scheme". In Fig. 6.3, we show the contour plots of the water surface computed by both schemes at time $t = 10$. It can be clearly observed that while the "new scheme" preserves the "lake at rest" steady states, the "old scheme" generates spurious oscillations on the quiescent lake surface.

In Fig. 6.4, we show the computed velocities u and v. Once again, while the velocities computed by the "new scheme"

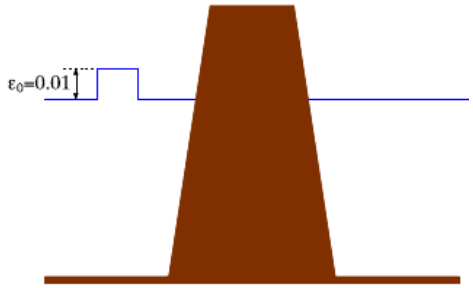

Fig. 6.5. Example 4: 1-D slice of the bottom topography and water surface. The plot is not to scale.

Example 4—Small perturbation of the "lake at rest" steady state

In this example, we solve the initial value problem, which is a modification of the test problem proposed in [7]. We define a hump partially submerged in water so that there is a disk-shaped island at the origin; see Fig. 6.5.

In this example, we take the computational domain $[0,1]\times[0,1]$ (divided into 25600 triangular cells), the radially symmetric bottom topography

$$B(r)=\begin{cases}1.1, & r\le 0.1,\\ 11(0.2-r), & 0.1<r\le 0.2,\\ 0, & \text{otherwise},\end{cases}\qquad r:=\sqrt{(x-0.5)^2+(y-0.5)^2},$$

the initial data

$$w(x,y,0)=\begin{cases}1+\varepsilon_0, & 0.1\le x\le 0.2,\\ \max[1,B(r)], & \text{otherwise},\end{cases}\qquad u(x,y,0)\equiv v(x,y,0)\equiv 0$$

with $\varepsilon_0=0.01$, and the homogeneous Neumann boundary conditions.

We then simulate a small perturbation that travels on initial quiescent water surface around the island using both the "new" and "old" schemes and plot the water surface computed at times $t=0.06$, 0.1, 0.14 and 0.2 in Fig. 6.6. As one can clearly see there, in the results obtained using the "old scheme" (see the right column of Fig. 6.6), spurious waves are generated in the cells at the wet/dry front and then they are spread outwards interacting with the right-going perturbation (notice that a much larger number of triangular cells was used in [7]to suppress the developed spurious waves). In contrast, as one can see in the left column of Fig. 6.6, such spurious waves are completely eliminated by using the "new scheme" even on a very coarse mesh. This clearly demonstrates the advantage of the "new scheme".

Example 5—Oscillating lake in a parabolic basin

In this example, water sloshing in a frictionless parabolic basin involves simultaneously wetting and drying. The bottom topography is defined by

$$B(x,y)=\frac{h_s}{L^2}(x^2+y^2) \tag{6.1}$$

where h_s and L are positive parameters. As it was shown in [43], the system (1.1)–(1.3), (6.1) admits the following periodic solution:

$$\begin{aligned}&w(x,y,t)=h_s\left[1+\frac{\phi}{L^2}(2x\cos(\omega t)+2y\sin(\omega t)-\phi)\right],\\ &u(x,y,t)=-\phi\,\omega\sin(\omega t),\quad v(x,y,t)=-\phi\,\omega\cos(\omega t),\end{aligned} \tag{6.2}$$

where $\omega=2\pi/T$ is the frequency of the circulation and T is its period. We use the parameters given in [33], that is, $T=3600$, $h_s=10$, $L=8025.5$ and $\phi=L/10$. The water circulation is simulated in a $[-10000,10000]\times[-10000,10000]$ computational domain which is divided into 11714 triangular cells. The initial conditions at $t=0$ are provided by (6.2) computed at $t=0$ and the homogeneous Neumann boundary conditions are set.

Fig. 6.7 shows both the exact and computed water surfaces at times $t=1.25T$ and $1.75T$. As one can clearly see, they are in good agreement and no distortion is observed near the shorelines.

In Fig. 6.8, we plot the velocity components u and v as functions of time at the point $(x,y)=(1000,0)$ for three periods. It can be observed that for both u and v the numerical results agree very well with the exact solution. Fig. 6.8 also demonstrates the converges of the computed solution to the analytical one as both the coarse (with 5808 triangular cells)

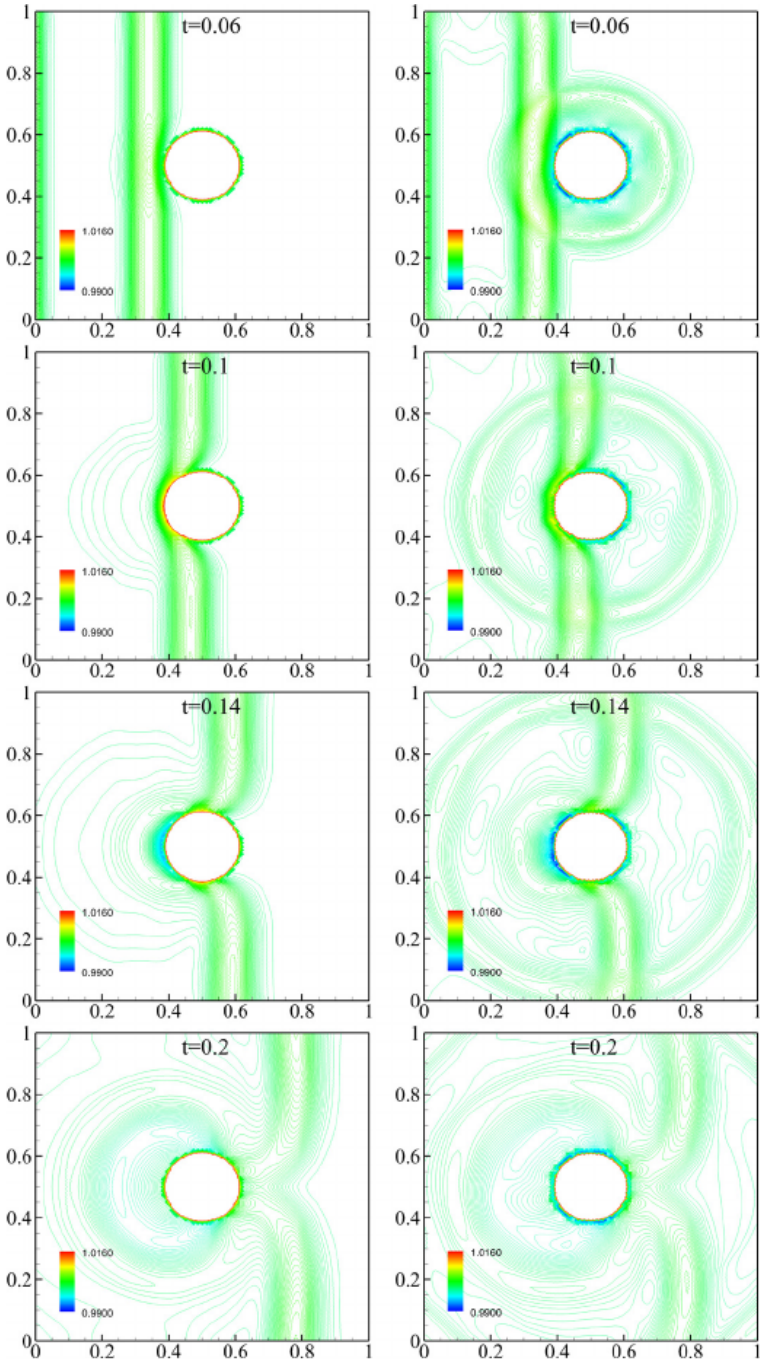

Fig. 6.6. Example 4: Water surface computed by the "new" (left column) and "old" (right column) schemes.

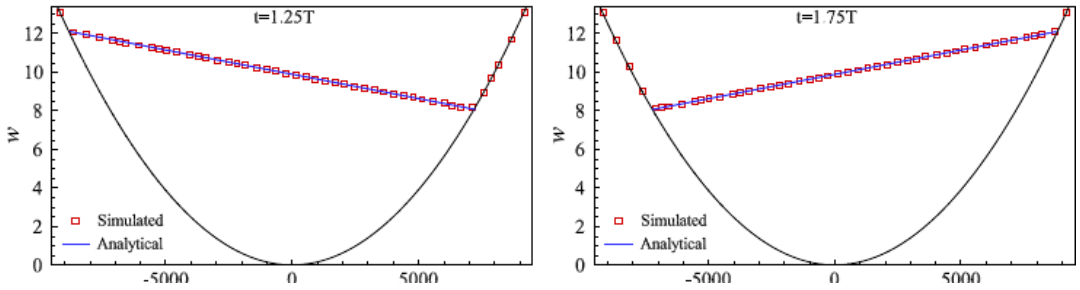

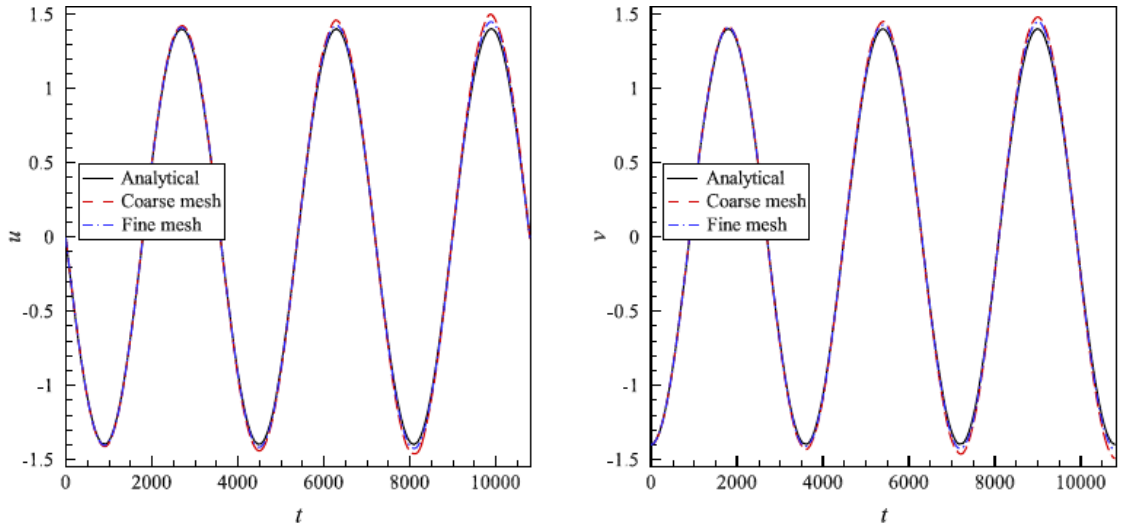

Fig. 6.8. Example 5: Simulated and analytical velocity components u and v at different times computed on the coarse and fine meshes.

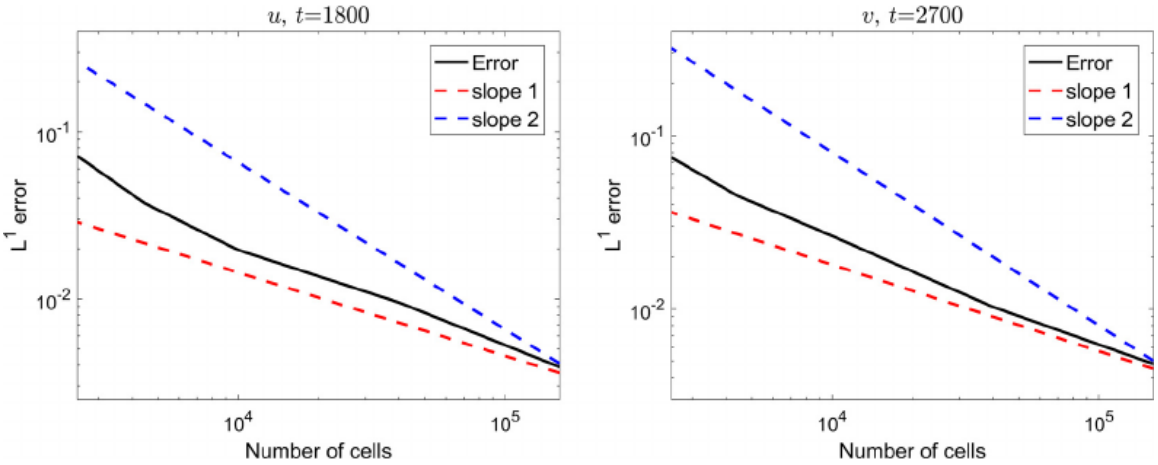

Fig. 6.9. Example 5: L^1-errors for u and v as functions of the number of triangular cells.

observe, the achieved experimental convergence rates (between 1 and 2) are comparable to those reported in the literature; see, e.g., [8,14,20].

Example 6—Dam-break wave propagating over irregular dry bed

In this example, we simulate a moving wet/dry front produced by a dam-break wave propagating over a frictional dry bed with three mounds. The dam-break is simulated in the $[0, 6] \times [0, 6]$ domain with the bottom topography defined by

$$B(x, y) = \max\left[0.5e^{-8(x-2)^2-10(y-3)^2}, 0.2e^{-3(x-4)^2-4(y-4.8)^2}, 0.2e^{-3(x-4)^2-4(y-1.2)^2}\right].$$

In order to take into account the friction effect, we add the Manning friction terms and modify the governing equations (1.2) and (1.3)as follows:

$$\begin{aligned}
&(hu)_t + \left(hu^2 + \frac{g}{2}h^2\right)_x + (huv)_y = -ghB_x - \frac{gn_b^2 u\sqrt{u^2+v^2}}{h^{1/3}},\\
&(hv)_t + (huv)_x + \left(hv^2 + \frac{g}{2}h^2\right)_y = -ghB_y - \frac{gn_b^2 v\sqrt{u^2+v^2}}{h^{1/3}},
\end{aligned} \tag{6.3}$$

where n_b is the Manning roughness coefficient. We take $n_b = 0.01$.

We numerically solve the system (1.1), (6.3)using the developed well-balanced positivity preserving semi-discrete central-upwind scheme. Due to the presence of friction terms, the resulting ODE system (2.1)is now stiff. We therefore integrate it using the steady state and sign preserving semi-implicit Runge–Kutta methods from [10]; see also [11].

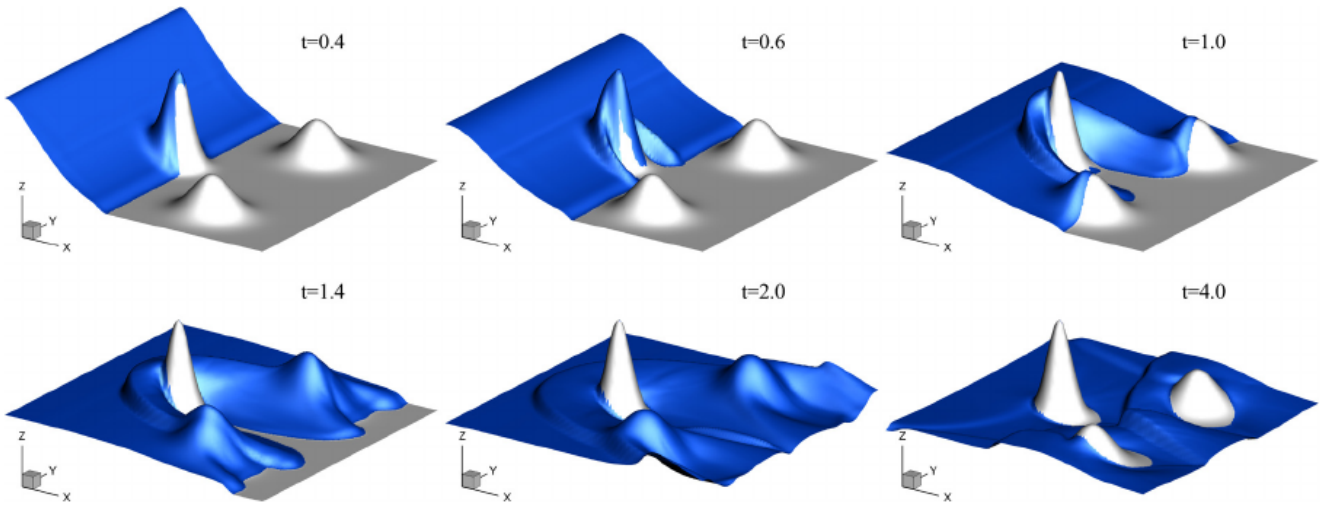

Fig. 6.10. Example 6: Simulated water surface at different times.

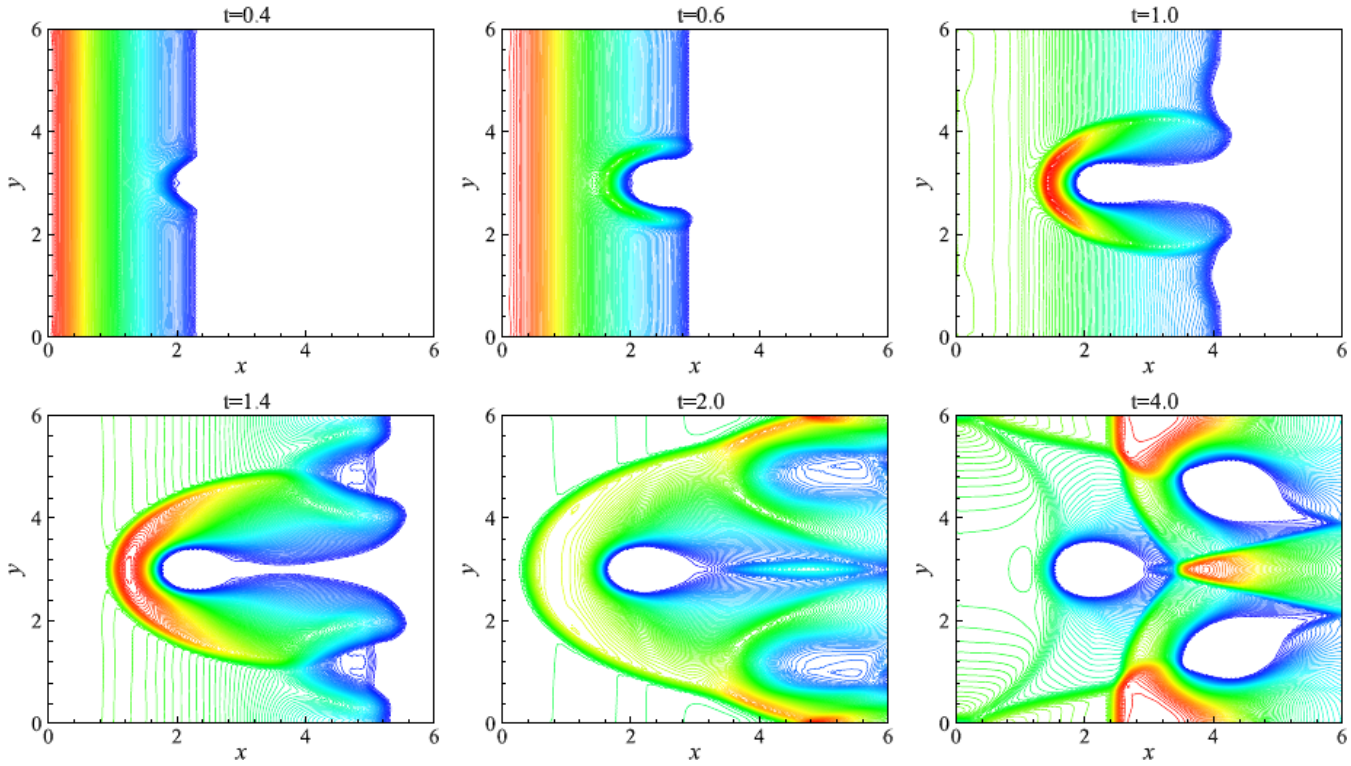

Fig. 6.11. Example 6: Simulated water depth at different times.

In Fig. 6.10, we show the 3-D view of the dam-break wave propagation over the initially dry bed at different times. It can be observed that the proposed scheme performs well when handling both wetting and drying processes. In Fig. 6.11, where the contour lines of the water depth computed at different times are plotted, the reflections and interactions of the waves can be clearly seen and no oscillations or disturbances are observed at the wet/dry boundaries.

Example 7—Two-dimensional solitary wave run-up on a conical island

In this example, we compare the proposed method with a laboratory experiment simulating a solitary wave that passes around a conical island. The laboratory experiments were performed at the Coastal and Hydraulics Laboratory (see [6]) and the measured data are compared with the simulated results. As described in [5,37], this experiment may not be an ideal test for the accuracy of developed numerical methods as the waves generated in the laboratory are dispersive. However, it can be used to test the robustness of the numerical methods for simulating long wave run-up on arbitrary 2-D topography

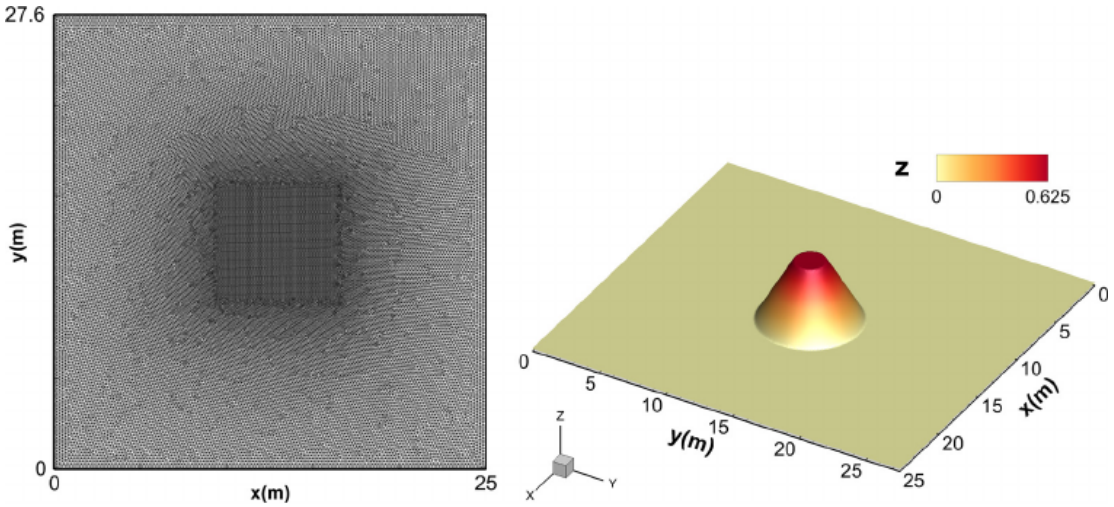

Fig. 6.12. Example 7: Triangular grid (left) and the bottom topography profile (right).

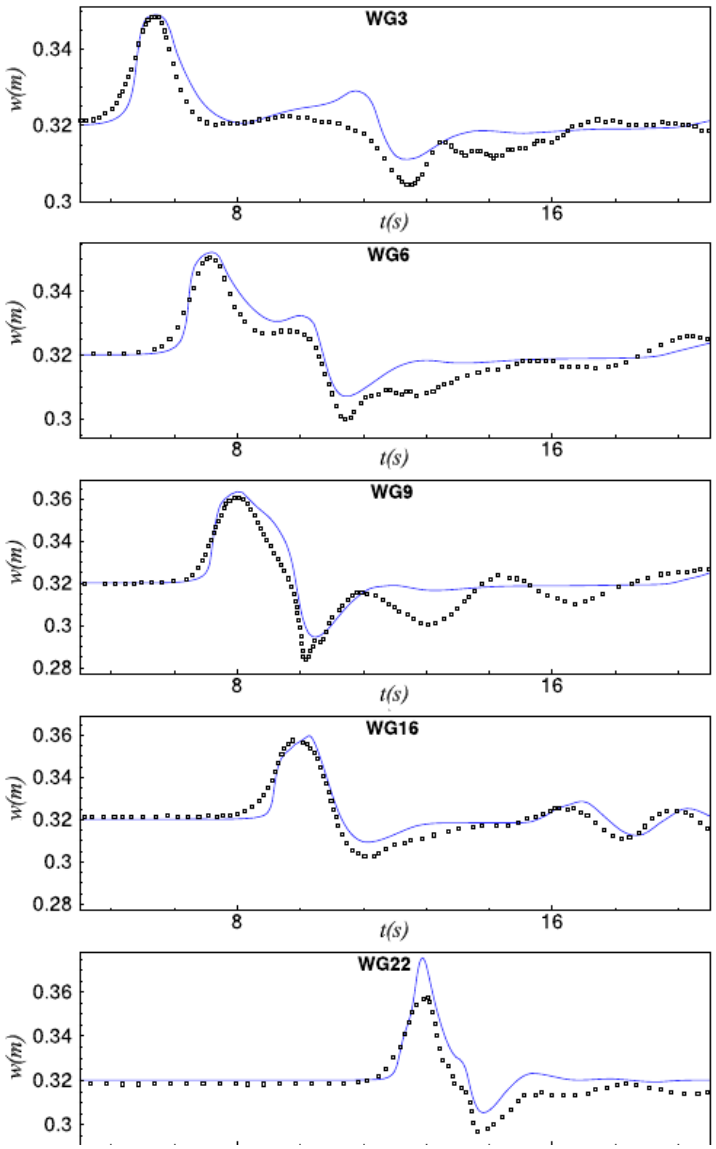

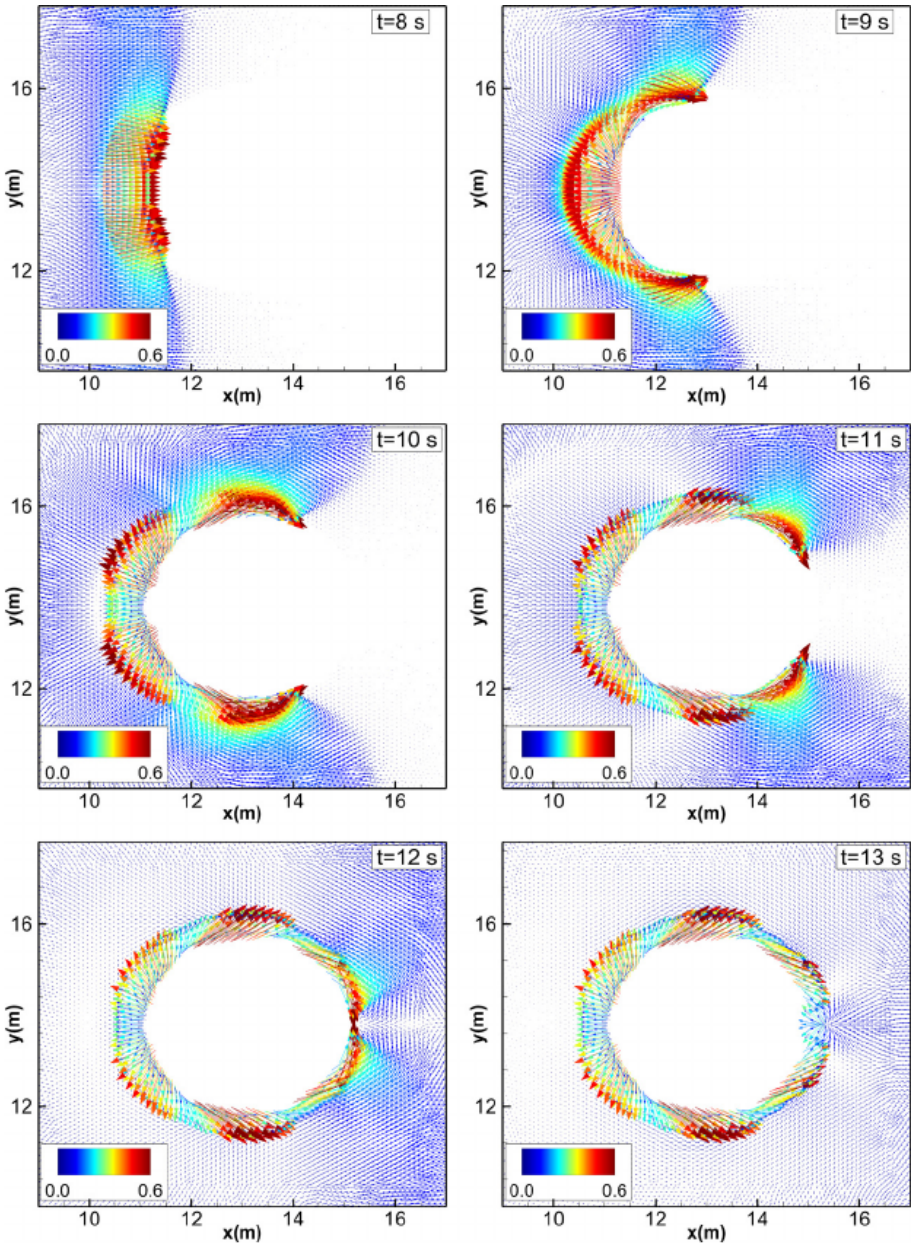

Fig. 6.14. Example 7: Simulated velocity vectors around the conical island at different times.

$$B(r) = \begin{cases} 0.625, & r \le 1.1, \\ 0.25(3.6 - r), & 1.1 < r \le 3.6, \\ 0, & \text{otherwise}, \end{cases} \qquad r := \sqrt{(x - 12.96)^2 + (y - 13.8)^2};$$

see Fig. 6.12 (right). The computational domain $[25 \times 27.6]$ is divided into 72152 triangular cells with the grid refined in the island area as shown in Fig. 6.12 (left).

In the numerical test, the initial conditions correspond to the "lake at rest" with

$$w(x, y, 0) = \max\{D, B(x, y)\}, \quad u(x, y, 0) \equiv v(x, y, 0) \equiv 0,$$

where $D = 0.32$ m. The boundaries at $y = 0$ and $y = 27.6$ are set to be reflecting (solid wall), the boundary at $x = 25$ is set to be outflow, and an inflow boundary at $x = 0$ is set to replicate the wave-maker produced planar solitary wave:

$$w(0, y, t) = D + H_w \operatorname{sech}^2\left[\sqrt{\frac{3H_w}{4D^3}}\, C(t - T)\right], \quad u(0, y, t) = C\left(1 - \frac{D}{w(0, y, t)}\right), \quad v(0, y, t) = 0,$$

We numerically simulate the initial run-up and run-down processes occurring within the first 20 s. In Fig. 6.13, we compare the computed and experimentally measured water surfaces as functions of time at the following five gauges: WG3(6.82, 13.05), WG6(9.36, 13.80), WG9(10.36, 13.80), WG16(12.96, 11.22) and WG22(15.56, 13.80). As one can see, the proposed numerical method is capable of simulating correct tendency of the water surface changes and arrival times. The agreement between the simulated and experimental data are satisfactory. Similar predicted results are observed in [5,21,37]. The discrepancies, especially the underestimation of the steepness of the wave, could be explained by the underprediction in the secondary depression wave which follows the main wave; see [37].

In Fig. 6.14, we show the velocity vectors computed at different times when the wave passes around the conical island. As one can clearly see, no oscillations or artificially large velocity magnitudes are generated at the wave front during the wetting–drying process. This verifies the robustness of the proposed numerical method.

7. Conclusion

In this paper, we have developed a new "truly" well-balanced positivity preserving semi-discrete central-upwind scheme for the 2-D Saint-Venant system of shallow water equations. The well-balanced and positivity preserving properties are ensured with the help of a novel wet/dry water surface reconstruction on unstructured triangular grids. In partially flooded cells, the proposed reconstruction is based on a subcell resolution and may consist of two linear pieces designed to accurately approximate the wet/dry interface within the cell. In addition, the use of the new wet/dry reconstruction requires a special discretization of the source term, which has been developed to guarantee that the resulting scheme is well-balanced. The positivity of the computed water depth has been enforced using a "draining" time-step technique. We have performed several numerical experiments designed to demonstrate the ability of the proposed scheme to capture involving wet/dry interfaces in a stable, non-oscillatory manner.

Acknowledgements

The work of A. Kurganov was supported in part by the NSF grant DMS-1521009 and NSFC grant 11771201.

References

[1] E. Audusse, F. Bouchut, M.-O. Bristeau, R. Klein, B. Perthame, A fast and stable well-balanced scheme with hydrostatic reconstruction for shallow water flows, SIAM J. Sci. Comput. 25 (2004) 2050–2065.
[2] A. Beljadid, A. Mohammadian, A. Kurganov, Well-balanced positivity preserving cell-vertex central-upwind scheme for shallow water flows, Comput. Fluids 136 (2016) 193–206.
[3] A. Bollermann, G. Chen, A. Kurganov, S. Noelle, A well-balanced reconstruction of wet/dry fronts for the shallow water equations, J. Sci. Comput. 56 (2013) 267–290.
[4] A. Bollermann, S. Noelle, M. Lukáčová-Medviďová, Finite volume evolution Galerkin methods for the shallow water equations with dry beds, Commun. Comput. Phys. 10 (2011) 371–404.
[5] S.F. Bradford, B.F. Sanders, Finite-volume model for shallow-water flooding of arbitrary topography, J. Hydraul. Eng. 128 (2002) 289–298.
[6] M.J. Briggs, C.E. Synolakis, G.S. Harkins, D.R. Green, Laboratory experiments of tsunami runup on a circular island, Pure Appl. Geophys. 144 (1995) 569–593.
[7] S. Bryson, Y. Epshteyn, A. Kurganov, G. Petrova, Well-balanced positivity preserving central-upwind scheme on triangular grids for the Saint-Venant system, M2AN Math. Model. Numer. Anal. 45 (2011) 423–446.
[8] S. Bunya, E.J. Kubatko, J.J. Westerink, C. Dawson, A wetting and drying treatment for the Runge–Kutta discontinuous Galerkin solution to the shallow water equations, Comput. Methods Appl. Mech. Eng. 198 (2009) 1548–1562.
[9] M. Castro, J.M. Gallardo, C. Parés, High order finite volume schemes based on reconstruction of states for solving hyperbolic systems with nonconservative products. Applications to shallow-water systems, Math. Comput. 75 (2006) 1103–1134.
[10] A. Chertock, S. Cui, A. Kurganov, W. Tong, Steady state and sign preserving semi-implicit Runge–Kutta methods for ODEs with stiff damping term, SIAM J. Numer. Anal. 53 (2015) 1987–2008.
[11] A. Chertock, S. Cui, A. Kurganov, T. Wu, Well-balanced positivity preserving central-upwind scheme for the shallow water system with friction terms, Int. J. Numer. Methods Fluids 78 (2015) 355–383.
[12] B.H. Choi, D.C. Kim, E. Pelinovsky, S.B. Woo, Three-dimensional simulation of tsunami run-up around conical island, Coast. Eng. 54 (2007) 618–629.
[13] A.J.C. de Saint-Venant, Thèorie du mouvement non-permanent des eaux, avec application aux crues des rivière at à l'introduction des marèes dans leur lit, C. R. Acad. Sci. Paris 73 (1871) 147–154.
[14] A. Ern, S. Piperno, K. Djadel, A well-balanced Runge–Kutta discontinuous Galerkin method for the shallow-water equations with flooding and drying, Int. J. Numer. Methods Fluids 58 (2008) 1–25.
[15] U.S. Fjordholm, S. Mishra, E. Tadmor, Well-balanced and energy stable schemes for the shallow water equations with discontinuous topography, J. Comput. Phys. 230 (2011) 5587–5609.
[16] J.M. Gallardo, C. Parés, M. Castro, On a well-balanced high-order finite volume scheme for shallow water equations with topography and dry areas, J. Comput. Phys. 227 (2007) 574–601.
[17] T. Gallouët, J.-M. Hérard, N. Seguin, Some approximate Godunov schemes to compute shallow-water equations with topography, Comput. Fluids 32 (2003) 479–513.
[18] S. Gottlieb, D. Ketcheson, C.-W. Shu, Strong Stability Preserving Runge–Kutta and Multistep Time Discretizations, World Scientific Publishing Co. Pte. Ltd., Hackensack, NJ, 2011.
[19] S. Gottlieb, C.-W. Shu, E. Tadmor, Strong stability-preserving high-order time discretization methods, SIAM Rev. 43 (2001) 89–112.

[22] P. Jawahar, H. Kamath, A high-resolution procedure for Euler and Navier–Stokes computations on unstructured grids, J. Comput. Phys. 164 (2000) 165–203.
[23] S. Jin, A steady-state capturing method for hyperbolic systems with geometrical source terms, M2AN Math. Model. Numer. Anal. 35 (2001) 631–645.
[24] A. Kurganov, D. Levy, Central-upwind schemes for the Saint-Venant system, M2AN Math. Model. Numer. Anal. 36 (2002) 397–425.
[25] A. Kurganov, C.-T. Lin, On the reduction of numerical dissipation in central-upwind schemes, Commun. Comput. Phys. 2 (2007) 141–163.
[26] A. Kurganov, S. Noelle, G. Petrova, Semi-discrete central-upwind scheme for hyperbolic conservation laws and Hamilton–Jacobi equations, SIAM J. Sci. Comput. 23 (2001) 707–740.
[27] A. Kurganov, G. Petrova, Central-upwind schemes on triangular grids for hyperbolic systems of conservation laws, Numer. Methods Partial Differ. Equ. 21 (2005) 536–552.
[28] A. Kurganov, G. Petrova, A second-order well-balanced positivity preserving central-upwind scheme for the Saint-Venant system, Commun. Math. Sci. 5 (2007) 133–160.
[29] A. Kurganov, M. Prugger, T. Wu, Second-order fully discrete central-upwind scheme for two-dimensional hyperbolic systems of conservation laws, SIAM J. Sci. Comput. 39 (2017) A947–A965.
[30] A. Kurganov, E. Tadmor, New high resolution central schemes for nonlinear conservation laws and convection–diffusion equations, J. Comput. Phys. 160 (2000) 241–282.
[31] A. Kurganov, E. Tadmor, Solution of two-dimensional Riemann problems for gas dynamics without Riemann problem solvers, Numer. Methods Partial Differ. Equ. 18 (2002) 584–608.
[32] R.J. LeVeque, Balancing source terms and flux gradients in high-resolution Godunov methods: the quasi-steady wave-propagation algorithm, J. Comput. Phys. 146 (1998) 346–365.
[33] Q. Liang, Flood simulation using a well-balanced shallow flow model, J. Hydraul. Eng. 136 (2010) 669–675.
[34] P.L.-F. Liu, Y.-S. Cho, M.J. Briggs, U. Kanoglu, C.E. Synolakis, Runup of solitary waves on a circular island, J. Fluid Mech. 302 (1995) 259–285.
[35] X. Lu, B. Dong, B. Mao, X. Zhang, A two-dimensional depth-integrated non-hydrostatic numerical model for nearshore wave propagation, Ocean Model. 96 (2015) 187–202.
[36] P.J. Lynett, T.-R. Wu, P.L.-F. Liu, Modeling wave runup with depth-integrated equations, Coast. Eng. 46 (2002) 89–107.
[37] I.K. Nikolos, A.I. Delis, An unstructured node-centered finite volume scheme for shallow water flows with wet–dry fronts over complex topography, Comput. Methods Appl. Mech. Eng. 198 (2009) 3723–3750.
[38] S. Noelle, N. Pankratz, G. Puppo, J.R. Natvig, Well-balanced finite volume schemes of arbitrary order of accuracy for shallow water flows, J. Comput. Phys. 213 (2006) 474–499.
[39] B. Perthame, C. Simeoni, A kinetic scheme for the Saint-Venant system with a source term, Calcolo 38 (2001) 201–231.
[40] M. Ricchiuto, An explicit residual based approach for shallow water flows, J. Comput. Phys. 280 (2015) 306–344.
[41] G. Russo, A. Khe, High order well-balanced schemes based on numerical reconstruction of the equilibrium variables, in: Proceedings of the 15th Conference on Waves and Stability in Continuous Media, WASCOM 2009, World Sci. Publ., Hackensack, NJ, 2010, pp. 230–241.
[42] H. Shirkhani, A. Mohammadian, O. Seidou, A. Kurganov, A well-balanced positivity-preserving central-upwind scheme for shallow water equations on unstructured quadrilateral grids, Comput. Fluids 126 (2016) 25–40.
[43] W.C. Thacker, Some exact solutions to the nonlinear shallow-water wave equations, J. Fluid Mech. 107 (1981) 499–508.
[44] V.V. Titov, C.E. Synolakis, Modeling of breaking and nonbreaking long-wave evolution and runup using VTCS-2, J. Waterw. Port Coast. 121 (1995) 308–316.
[45] V.V. Titov, C.E. Synolakis, Numerical modeling of tidal wave runup, J. Waterw. Port Coast. 124 (1998) 157–171.
[46] Y. Xing, C.-W. Shu, A survey of high order schemes for the shallow water equations, J. Math. Study 47 (2014) 221–249.
[47] Y. Xing, X. Zhang, C.-W. Shu, Positivity-preserving high order well-balanced discontinuous Galerkin methods for the shallow water equations, Adv. Water Resour. 33 (2010) 1476–1493.